PHYSICAL REVIEW D **92,** 094511 (2015)

Isovector and isoscalar tensor charges of the nucleon from lattice QCD

Tanmoy Bhattacharya,[1,*] Vincenzo Cirigliano,[1,†] Saul D. Cohen,[2,‡] Rajan Gupta,[1,§] Anosh Joseph,[3,‖] Huey-Wen Lin,[4,¶] and Boram Yoon[1,**]

(Precision Neutron Decay Matrix Elements (PNDME) Collaboration)

[1]*Los Alamos National Laboratory, Theoretical Division T-2, Los Alamos, New Mexico 87545, USA*
[2]*Institute for Nuclear Theory, University of Washington, Seattle, Washington 98195, USA*
[3]*John von Neumann Institute for Computing, DESY, 15738 Zeuthen, Germany*
[4]*Physics Department, University of California, Berkeley, California 94720, USA*

(Received 9 July 2015; published 10 November 2015)

We present results for the isovector and flavor diagonal tensor charges g_T^{u-d}, g_T^u, g_T^d, and g_T^s needed to probe novel tensor interactions at the TeV scale in neutron and nuclear β-decays and the contribution of the quark electric dipole moment (EDM) to the neutron EDM. The lattice QCD calculations were done using nine ensembles of gauge configurations generated by the MILC collaboration using the HISQ action with $2+1+1$ dynamical flavors. These ensembles span three lattice spacings $a \approx 0.06$, 0.09 and 0.12 fm and three quark masses corresponding to the pion masses $M_\pi \approx 130$, 220 and 310 MeV. Using estimates from these ensembles, we quantify all systematic uncertainties and perform a simultaneous extrapolation in the lattice spacing, volume and light quark masses for the connected contributions. The final estimates of the connected nucleon (proton) tensor charge for the isovector combination is $g_T^{u-d} = 1.020(76)$ in the $\overline{\text{MS}}$ scheme at 2 GeV. The additional disconnected quark loop contributions needed for the flavor-diagonal matrix elements are calculated using a stochastic estimator employing the truncated solver method with the all-mode-averaging technique. We find that the size of the disconnected contribution is smaller than the statistical error in the connected contribution. This allows us to bound the disconnected contribution and include it as an additional uncertainty in the flavor-diagonal charges. After a continuum extrapolation, we find $g_T^u = 0.774(66)$, $g_T^d = -0.233(28)$ and $g_T^{u+d} = 0.541(67)$. The strangeness tensor charge, that can make a significant contribution to the neutron EDM due to the large ratio $m_s/m_{u,d}$, is $g_T^s = 0.008(9)$ in the continuum limit.

DOI: 10.1103/PhysRevD.92.094511 PACS numbers: 11.15.Ha, 12.38.Gc

I. INTRODUCTION

Precise estimates of the matrix elements of the isoscalar and isovector tensor bilinear quark operators are needed to obtain bounds on new physics from precision measurements of β-decays and limits on the neutron electric dipole moment (nEDM). The isovector charge, g_T^{u-d}, is needed to probe novel tensor interactions in the helicity-flip part of the neutron decay distribution [1] while the isoscalar charges are needed to quantify the contribution of the quark EDM to the nEDM and set bounds on new sources of CP violation. In this paper, we give details of the simulations of lattice QCD using the clover-on-HISQ approach to provide first principle estimates of these matrix elements with control over all sources of systematic errors.

Lattice QCD analysis of isovector charges of nucleons is well developed (See the recent reviews [2–4]). In this work we present precise estimates of this dominant contribution, given by the connected diagrams, to the tensor charges, i.e., the insertion of the zero-momentum tensor operator in one of the three valence quarks in the nucleon. Calculation of the isoscalar charges is similar except that it gets additional contributions from contractions of the operator as a vacuum quark loop. This is called the disconnected contribution as the quark loop and nucleon propagator interact only through the exchange of gluons. The statistical signal in the disconnected term is weak, so it is computationally much more expensive. We find, on the four ensembles analyzed, that the disconnected contributions of light quarks are small and in most cases are consistent with zero within errors. We, therefore, use the largest of these estimates to bound the disconnected contribution and include it as a systematic uncertainty in the presentation of the final results. Similarly, using five ensembles we show that the disconnected contribution of the strange quark, also needed for the nEDM analysis, is even smaller but we are able to extract a continuum limit estimate [5].

Throughout the paper, we present results for the tensor charges of the proton, which by convention are called nucleon tensor charges in literature. Results for the neutron are obtained by the $u \leftrightarrow d$ interchange. This paper is

*tanmoy@lanl.gov
†cirigliano@lanl.gov
‡saul.cohen@gmail.com
§rajan@lanl.gov
‖anosh.joseph@desy.de
¶hueywenlin@lbl.gov
**boram@lanl.gov

organized as follows. In Sec. II, we describe the parameters of the gauge ensembles analyzed, the lattice methodology, fits used to extract matrix elements within the ground state of the nucleon and the renormalization of the operators. We discuss the calculation of the connected diagram in Sec. III, and of the disconnected contribution in Sec. IV. Our final results are presented in Sec. V and we end with conclusions in Sec. VI. In the Appendix we present a summary of the control over systematics of existing lattice calculations using the FLAG quality criteria [6].

II. LATTICE PARAMETERS AND METHODOLOGY

In this section we provide an overview of the calculational details. These include a description of the gauge ensembles analyzed, a short review of the operators used to calculate the two-point and three-point correlation functions using clover fermions, the fit ansatz used to extract the desired matrix elements from the correlation functions and estimates of renormalization constants using the RI-sMOM scheme.

A. Lattice parameters

In order to obtain estimates with a desired precision, it is important to quantify all sources of systematic errors. For matrix elements between nucleon ground states, these include excited state contamination, finite lattice volume, operator renormalization, discretization effects at finite lattice spacing and extrapolations from heavier u and d quarks. Since lattice generation is very expensive, it was, therefore, expedient to use a set of existing gauge ensembles that cover a sufficiently large range in lattice spacing and light quark mass to study the continuum and chiral behavior. The only set available to us that meets our requirements are the ensembles generated using $N_f = 2+1+1$ flavors of highly improved staggered quarks (HISQ) [7] by the MILC collaboration [8]. The parameters of the nine ensembles used in this study are given in Table I. In this paper we show that these ensembles allow us to address issues of statistics, excited state contamination, lattice volume, lattice spacing and the chiral behavior in the calculation of the tensor charges.

Staggered fermions have the advantage of being computationally cheaper and preserve an important remnant of the continuum chiral symmetry. Their disadvantage is that the spectrum has a four-fold doubling in the continuum limit. This doubling symmetry (called the taste symmetry) is broken at finite lattice spacing and this breaking introduces additional lattice artifacts. Due to taste mixing, staggered baryon interpolating operators couple, in general, to a combination of octet (the nucleon) and the decuplet (Delta) states. Furthermore, these baryon operators couple to both parity states in addition to all radial excitations of these. Thus, baryon correlation functions are more complicated to analyze compared to Wilson-type fermions, as they have a weaker statistical signal, the consequences of taste mixing has to be resolved and one has to take into account the oscillating signal due to contributions from both parity states. Since having a good statistical signal is a prerequisite to quantifying the various sources of systematic errors, we have chosen to construct correlation functions using Wilson-clover fermions, as these preserve the continuum spin structure. This mixed-action, clover-on-HISQ, approach, however, leads to a nonunitary lattice formulation and at small, but *a priori* unknown, quark masses suffers from the problem of exceptional configurations discussed next.

TABLE I. Parameters of the $(2+1+1)$ flavor HISQ lattices generated by the MILC collaboration and analyzed in this study are quoted from Ref. [8]. Symbols used in plots are defined along with the ensemble ID. Finite size effects are analyzed in terms of $M_\pi L$ with the clover-on-HISQ M_π defined in Table II.

Ensemble ID		a (fm)	$M_\pi^{\rm sea}$ (MeV)	$L^3 \times T$	$M_\pi L$
a12m310	△	0.1207(11)	305.3(4)	$24^3 \times 64$	4.55
a12m220S	◁	0.1202(12)	218.1(4)	$24^3 \times 64$	3.29
a12m220	▷	0.1184(10)	216.9(2)	$32^3 \times 64$	4.38
a12m220L	▽	0.1189(09)	217.0(2)	$40^3 \times 64$	5.49
a09m310	✧	0.0888(08)	312.7(6)	$32^3 \times 96$	4.51
a09m220	☆	0.0872(07)	220.3(2)	$48^3 \times 96$	4.79
a09m130	⬡	0.0871(06)	128.2(1)	$64^3 \times 96$	3.90
a06m310	□	0.0582(04)	319.3(5)	$48^3 \times 144$	4.52
a06m220	◇	0.0578(04)	229.2(4)	$64^3 \times 144$	4.41

Exceptional configurations are ones in which the clover Dirac operator evaluated on HISQ configurations has near zero modes. As a result, on such configurations the inversion of the clover Dirac operator, which gives the Feynman propagator, can fail to converge and/or the corresponding correlation functions have an exceptionally large amplitude depending on the proximity to the zero mode. The presence of exceptional configurations biases the results or gives rise to unphysically large fluctuations and invalidates the results. In any lattice analysis based on a unitary formulation, such as HISQ-on-HISQ or clover-on-clover, such configurations are suppressed in the lattice generation. Given an appropriately generated ensemble of HISQ configurations, there is no basis for excluding any configuration from the ensemble average in a clover-on-HISQ calculation. Thus, these calculations should be done only on ensembles without any exceptional configurations.

The presence of such exceptional configurations in a clover-on-HISQ analysis is expected to increase on decreasing the quark mass at fixed lattice spacing and increase with the lattice spacing at fixed quark mass, i.e., the coarser the configurations, the more likely they are. Consequently, smearing techniques used to reduce short distance lattice artifacts also reduce the probability of encountering exceptional configurations. To reduce lattice

artifacts, we applied hypercubic (HYP) smearing [9] to all HISQ configurations. To check for exceptional configurations on these HYP smeared lattices, we monitor the convergence of the quark propagator and the size of fluctuations in correlations functions on each configuration. These tests provided evidence for exceptional configurations on the $a = 0.15$ fm ensembles and on the $a = 0.12$ fm ensemble with $M_\pi \approx 130$ MeV. Consequently, these ensembles, also generated by the MILC collaboration, were excluded from our analysis. An earlier discussion regarding exceptional configurations on these ensembles is given in Ref. [10]. To reiterate, the nine ensembles used in this study and described in Table I did not present evidence of an exceptional configuration.

The parameters used in the analysis with clover fermions are given in Table II. The Sheikholeslami-Wohlert coefficient used in the clover action is fixed to its tree-level value with tadpole improvement, $c_{\rm sw} = 1/u_0^3$ where u_0 is the tadpole factor of the HYP smeared HISQ lattices.

The masses of light clover quarks were tuned so that the clover-on-HISQ pion masses M_π (see Table II) match the HISQ-on-HISQ Goldstone ones, $M_\pi^{\rm sea}$, given in Table I. The strange quark mass m_s is tuned so that the resulting clover-on-HISQ $M_{s\bar{s}} = \sqrt{m_s^b/m_l^b} M_\pi^{\rm sea}$, where m_s^b/m_l^b is the ratio of bare strange and light quark masses used in the HISQ generation, and is 5 for m310 lattices, 10 for m220 lattices and 27 for m130 lattices. The resulting estimates for m_s are consistent with those obtained by matching to the kaon mass [11].

All fits in M_π^2 to study the chiral behavior are made using the clover-on-HISQ M_π^2 as correlation functions and thus the observables have a greater sensitivity to it. Performing fits using the HISQ-on-HISQ values of $M_\pi^{\rm sea2}$ did not change the estimates significantly.

Estimates of nucleon charges and form-factors based on lower statistics subset of data presented here for the two ensembles *a12m310* and *a12m220* have been published in [10]. Results for the tensor charges presented in this paper supersede those earlier estimates.

B. Lattice methodology

The two-point and three-point nucleon correlation functions at zero momentum are defined as

$$C^{\rm 2pt}_{\alpha\beta}(t) = \sum_{\mathbf{x}} \langle 0|\chi_\alpha(t,\mathbf{x})\bar{\chi}_\beta(0,\mathbf{0})|0\rangle, \quad (1)$$

$$C^{\rm 3pt}_{\Gamma;\alpha\beta}(t,\tau) = \sum_{\mathbf{x},\mathbf{x}'} \langle 0|\chi_\alpha(t,\mathbf{x})\mathcal{O}_\Gamma(\tau,\mathbf{x}')\bar{\chi}_\beta(0,\mathbf{0})|0\rangle, \quad (2)$$

where α and β are the spinor indices. The source time slice is translated to $t_0 = 0$, t is the sink time slice, and τ is the time slice at which the bilinear operator $\mathcal{O}^q_\Gamma(x) = \bar{q}(x)\Gamma q(x)$ is inserted. The Dirac matrix Γ is 1, γ_4, $\gamma_i\gamma_5$ and $\gamma_i\gamma_j$ for scalar (S), vector (V), axial (A) and tensor (T) operators, respectively. In this paper, subscripts i and j on gamma matrices run over $\{1,2,3\}$, with $i < j$. The interpolating operator used to create/annihilate the nucleon state, χ, is

$$\chi(x) = \epsilon^{abc}\left[q_1^{aT}(x) C\gamma_5 \frac{1}{2}(1 \pm \gamma_4) q_2^b(x)\right] q_1^c(x) \quad (3)$$

with color indices $\{a,b,c\}$, charge conjugation matrix C, and q_1 and q_2 denoting the two different flavors of light quarks. The nonrelativistic projection $(1 \pm \gamma_4)/2$ is inserted to improve the signal, with the plus and minus sign applied to the forward ($t > 0$) and backward ($t < 0$) propagation, respectively.

TABLE II. The parameters used in the calculation of clover propagators. The hopping parameter κ in the clover action is given by $2\kappa_{l,s} = 1/(m_{l,s} + 4)$. m_s is needed for the calculation of the strange quark disconnected loop diagram. The Gaussian smearing parameters are defined by $\{\sigma, N_{\rm KG}\}$ where $N_{\rm KG}$ is the number of applications of the Klein-Gordon operator and the width is controlled by the coefficient σ, in Chroma convention. Smearing parameters used in the study of disconnected diagrams are given within square-brackets. m_l is tuned to achieve $M_\pi = M_\pi^{\rm sea}$, and m_s is tuned so that $M_{s\bar{s}} = \sqrt{m_s^b/m_l^b} M_\pi^{\rm sea}$. The error in the pion mass M_π is governed mainly by the uncertainty in the lattice scale given in Table I.

ID	m_l	m_s	$c_{\rm SW}$	$M_\pi^{\rm val}$(MeV)	Smearing
a12m310	−0.0695	−0.018718	1.05094	310.2(2.8)	$\{5.5,70\}$ $[\{5.5,70\}]$
a12m220S	−0.075	⋯	1.05091	225.0(2.3)	$\{5.5,70\}$
a12m220	−0.075	−0.02118	1.05091	227.9(1.9)	$\{5.5,70\}$ $[\{5.5,70\}]$
a12m220L	−0.075	⋯	1.05091	227.6(1.7)	$\{5.5,70\}$
a09m310	−0.05138	−0.016075	1.04243	313.0(2.8)	$\{5.5,70\}$ $[\{6.0,80\}]$
a09m220	−0.0554	−0.01761	1.04239	225.9(1.8)	$\{5.5,70\}$ $[\{6.0,80\}]$
a09m130	−0.058	⋯	1.04239	138.1(1.0)	$\{5.5,70\}$
a06m310	−0.0398	−0.01841	1.03493	319.6(2.2)	$\{6.5,70\}$ $[\{6.5,80\}]$
a06m220	−0.04222	⋯	1.03493	235.2(1.7)	$\{5.5,70\}$

The nucleon charges g_Γ^q are defined as

$$\langle N(p,s)|\mathcal{O}_\Gamma^q|N(p,s)\rangle = g_\Gamma^q \bar{u}_s(p)\Gamma u_s(p) \tag{4}$$

with spinors satisfying

$$\sum_s u_s(\mathbf{p})\bar{u}_s(\mathbf{p}) = \not{p} + m_N. \tag{5}$$

These charges, g_Γ^q, can be extracted from the ratio of the projected three-point function to the two-point function for $t \gg \tau \gg 0$

$$R_\Gamma(t,\tau) \equiv \frac{\langle \mathrm{Tr}[\mathcal{P}_\Gamma C_\Gamma^{3\mathrm{pt}}(t,\tau)]\rangle}{\langle \mathrm{Tr}[\mathcal{P}_{2\mathrm{pt}} C^{2\mathrm{pt}}(t)]\rangle} \longrightarrow \frac{1}{8}\mathrm{Tr}[\mathcal{P}_\Gamma(1+\gamma_4)\Gamma(1+\gamma_4)]g_\Gamma^q. \tag{6}$$

Here $\mathcal{P}_{2\mathrm{pt}} = (1+\gamma_4)/2$ is used to project out the positive parity contribution and $\mathcal{P}_\Gamma$ is defined below. Note that the ratio in Eq. (6) becomes zero if Γ anticommutes with γ_4, so only $\Gamma = 1$, γ_4, $\gamma_i\gamma_5$ and $\gamma_i\gamma_j$ can survive. In this paper, we present results for only the tensor channel, for which we can demonstrate control over all systematic errors.

On inserting a bilinear quark operator between the nucleon states to construct the three-point function, one gets two classes of diagrams: (i) the bilinear operator is contracted with one of the three valence quarks in the nucleon, as shown in the left diagram of Fig. 1, and (ii) the bilinear operator is contracted into a quark loop that is correlated with the nucleon two-point function through the exchange of gluons, as shown in the right diagram of Fig. 1. These are called the connected and disconnected diagrams, respectively.

The disconnected part of Eq. (6) can be written as

$$R_\Gamma^{\mathrm{disc}}(t,\tau) = \left\langle \sum_{\mathbf{x}} \mathrm{Tr}[M^{-1}(\tau,\mathbf{x};\tau,\mathbf{x})\Gamma] \right\rangle - \frac{\langle \mathrm{Tr}[\mathcal{P}_\Gamma C^{2\mathrm{pt}}(t)]\sum_{\mathbf{x}}\mathrm{Tr}[M^{-1}(\tau,\mathbf{x};\tau,\mathbf{x})\Gamma]\rangle}{\langle \mathrm{Tr}[\mathcal{P}_{2\mathrm{pt}} C^{2\mathrm{pt}}(t)]\rangle}, \tag{7}$$

where M is the Dirac operator. Note that the first term of the right-hand side is zero when $\Gamma \neq 1$, so it does not contribute to the tensor charges. High precision measurements of Eq. (7) requires improving the signal in the second term, i.e., the correlation between the nucleon two-point functions $C^{2\mathrm{pt}}$ and the quark loop $\mathrm{Tr}[M^{-1}\Gamma]$ as discussed in Secs. IV A and IV B.

The charges g_Γ^q are extracted from the ratio R_Γ by appropriate choice of the projection operator $\mathcal{P}_\Gamma$. For the calculation of connected contribution we use a single projection operator $\mathcal{P}_\Gamma = \mathcal{P}_{2\mathrm{pt}}(1 + i\gamma_5\gamma_3)$ to extract all four tensor structures at the same time as the projection is done at the time of the calculation of the sequential propagator. For the disconnected diagram, the projection operator is part of the final trace with the two-point function, so there is no additional cost to using tensor specific projectors. We, therefore, use

$$\begin{aligned}
\mathcal{P}_1 &= \mathcal{P}_{2\mathrm{pt}}, \\
\mathcal{P}_{\gamma_i\gamma_5} &= \mathcal{P}_{2\mathrm{pt}}\gamma_5\gamma_i \quad (i = 1,2,3), \\
\mathcal{P}_{\gamma_1\gamma_2} &= \mathcal{P}_{2\mathrm{pt}}\gamma_5\gamma_3, \\
\mathcal{P}_{\gamma_2\gamma_3} &= \mathcal{P}_{2\mathrm{pt}}\gamma_5\gamma_1, \\
\mathcal{P}_{\gamma_1\gamma_3} &= \mathcal{P}_{2\mathrm{pt}}\gamma_2\gamma_5,
\end{aligned} \tag{8}$$

which make $R_\Gamma(t,\tau) \to g_\Gamma$ for $t \gg \tau \gg 0$ as they satisfy

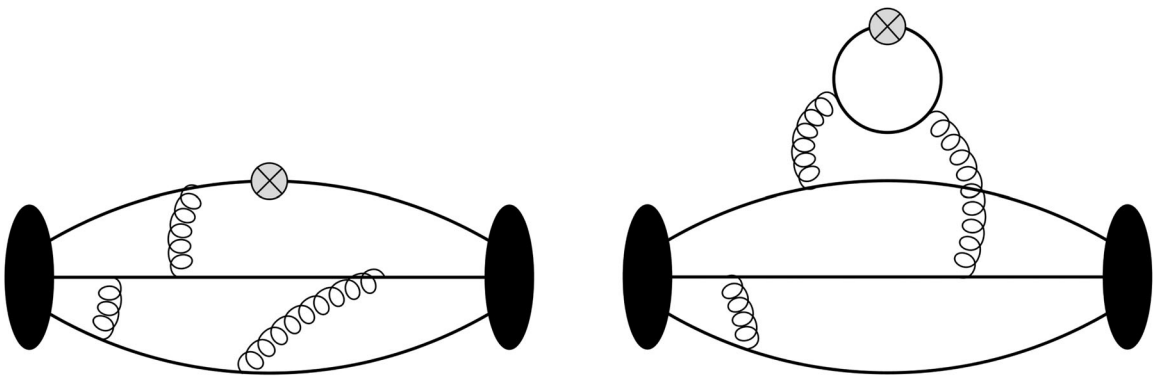

FIG. 1. The connected (left) and disconnected (right) three-point diagrams needed to calculate the matrix elements of bilinear quark operators in the nucleon state.

$$\frac{1}{8}\mathrm{Tr}[\mathcal{P}_\Gamma(1+\gamma_4)\Gamma(1+\gamma_4)] = 1. \quad (9)$$

For the disconnected diagrams, the statistics in the two-point function are improved by including the backward propagating baryons ($t < 0$) from each source point. In this case $\mathcal{P}^{2\mathrm{pt}} = (1-\gamma_4)/2$ is used to project out the negative parity state and we multiply the tensor projection operators $\mathcal{P}_{\gamma_i\gamma_j}$ in Eq. (8) by (-1) to match the convention used for forward propagation.

The calculation of the two-point and the connected three-point functions is carried out using the method described in our previous study, Ref. [10]. These calculations use the Chroma software package [12]. Part of the calculations are done on clusters with graphic processing units (GPUs) using QUDA library [13]. The source and sink baryon operators are constructed using smeared quark propagators to reduce the contamination from the excited states. We use gauge-invariant Gaussian smeared sources to improve the overlap with the ground state. Smearing is done by applying the three-dimensional Klein-Gordon operator ∇^2 a fixed number of times $(1-\sigma^2\nabla^2/(4N_{\mathrm{KG}}))^{N_{\mathrm{KG}}}$. The smearing parameters $\{\sigma, N_{\mathrm{KG}}\}$ for each ensemble are given in Table II.

To calculate the connected three-point function, we analyze configurations in sets of four measurements, i.e., we generate four independent propagators S_s^o on each configuration using smeared sources on four maximally separated time slices $t_{\mathrm{src}}^{i=1,4}$. For each S_s^o, the same smearing operation is applied at all time slices to create the smeared sink, and the two-point correlation function is calculated using these smeared-smeared propagators S_{ss}. Each of these four smeared propagators are used to construct sources for u and d quark propagators with the insertion of zero-momentum nucleon state at time slices displaced by a fixed t_{sep} from the four source time slices $t_{\mathrm{src}}^{i=1,4}$. These u and d sequential sources (generated separately) at $t_{\mathrm{src}}^{i=1,4} + t_{\mathrm{sep}}$ are smeared again. The final coherent sequential propagator S_c^{seq} is then calculated using the sum of these four smeared sources, i.e., the sequential propagator from the four time slices is calculated at one go. The connected three-point functions, over the four regions $t_{\mathrm{src}}^{i=1,4}$ to $t_{\mathrm{src}}^{i=1,4} + t_{\mathrm{sep}}$, are then constructed by inserting the bilinear operator between each of the original individual propagator S_s^o from $t_{\mathrm{src}}^{i=1,4}$ and the coherent sequential propagator S_c^{seq} from $t_{\mathrm{src}}^{i=1,4} + t_{\mathrm{sep}}$ [14]. The assumption one makes by adding the four sources to produce a single coherent sequential propagator is that the entire contribution to the three-point function in any one of the four intervals between $t_{\mathrm{src}}^{i=1,4}$ and $t_{\mathrm{src}}^{i=1,4} + t_{\mathrm{sep}}$ is from baryon insertion at $t_{\mathrm{src}}^{i} + t_{\mathrm{sep}}$ and the contribution of baryon sources at the other three time slices $t_{\mathrm{src}}^{j\neq i} + t_{\mathrm{sep}}$ in S_c^{seq} goes to zero on averaging over the gauge configurations. The coherent sequential source method has the advantage that the insertion of operators with different tensor structures and various momenta and for all four source positions can be done at the same time with tiny computational overhead.

TABLE III. The values of source-sink time separations (t_{sep}/a) used, the total number of configurations analyzed (N_{conf}) and measurements made (N_{meas}) for the two-point and connected three-point function calculations.

ID	t_{sep}/a	N_{conf}	N_{meas}
a12m310	{8, 9, 10, 11, 12}	1013	8104
a12m220S	{8, 10, 12}	1000	24000
a12m220	{8, 10, 12}	958	7664
a12m220L	10	1010	8080
a09m310	{10, 12, 14}	881	7048
a09m220	{10, 12, 14}	890	7120
a09m130	{10, 12, 14}	883	7064
a06m310	{16, 20, 22, 24}	1000	8000
a06m220	{16, 20, 22, 24}	650	2600

To study and quantify the excited state contamination, we repeat the calculation for multiple source-sink separations, t_{sep}. Separate sequential u and d propagators are calculated for each t_{sep} analyzed. Thus, the total number of inversions of the Dirac operator are $4 + 2 \times N_{t_{\mathrm{sep}}}$ for each set of four measurements on each configuration. Our choices of t_{sep} and the number of measurements made on each ensemble (number of configurations times the number of sources on each configuration) are given in Table III.

The calculation of disconnected quark loop diagrams using stochastic methods have a poor signal and requires very high statistics. Because of the computational cost, the calculations with light quarks have been done on the three heaviest, $M_\pi \approx 310$ MeV, and the *a12m220* ensembles; and on five ensembles for the strange quark as listed in Table VIII. For the evaluation of the disconnected diagrams, we obtain a stochastic estimate using the truncated solver method (TSM) [15,16] with the all-mode-averaging (AMA) technique [17] as described in Sec. IV.

C. Fits to correlation functions

To extract the desired nucleon charges, the matrix elements of the bilinear quark operators need to be calculated between ground state nucleons. On the lattice, however, any zero-momentum correlation function defined in Eq. (2) using the nucleon interpolation operator defined in (3), has a coupling to the ground state nucleon, all radially excited states, and multiparticle states with the same quantum numbers. Operators constructed using appropriately tuned smeared sources reduce the coupling to excited states but do not eliminate it. We discuss two synergistic strategies for removing the remaining excited state contamination based on the fact that in Euclidean time, the contributions from the excited states are exponentially suppressed as (i) the distance between the source/

TABLE IV. The nucleon ground and first excited state masses and the corresponding amplitudes obtained from a two-state fit to the nucleon two-point correlation function on each ensemble. The second set of estimates on the right are from an independent calculation performed to calculate the disconnected diagrams using the AMA with 64 LP measurements (96 LP for *a06m310*). All errors are estimated using the single-elimination Jackknife method using uncorrelated fits.

ID	Fit Range	aM_0	aM_1	$\mathcal{A}_0 \times 10^{11}$	$\mathcal{A}_1 \times 10^{11}$	Fit Range	aM_0	aM_1	$\mathcal{A}_0 \times 10^{11}$	$\mathcal{A}_1 \times 10^{11}$
a12m310	2–15	0.6669(53)	1.36(11)	6.57(27)	6.28(61)	2–15	0.6701(16)	1.471(45)	6.845(82)	6.88(35)
a12m220S	2–15	0.6233(55)	1.42(13)	6.58(26)	6.94(93)					
a12m220	2–15	0.6232(49)	1.45 (15)	6.58(24)	6.8(1.1)	2–15	0.6124(17)	1.294(37)	6.070(91)	6.34(23)
a12m220L	2–15	0.6046(71)	1.16(12)	5.68(37)	5.63(51)					
a09m310	3–20	0.4965(46)	0.938(57)	14.12(75)	17.4(1.1)	3–20	0.4973(12)	0.971(22)	2.215(31)	2.374(74)
a09m220	3–20	0.4554(45)	0.925(53)	12.13(61)	18.5(1.3)	3–20	0.4524(24)	0.877(34)	1.812(56)	2.29(10)
a09m130	3–20	0.4186(76)	0.834(61)	9.74(89)	17.2(1.0)					
a06m310	4–30	0.3245(30)	0.617(18)	0.566(30)	1.439(42)	4–30	0.3283(15)	0.630(10)	0.609(15)	1.513(29)
a06m220	5–30	0.3166(66)	0.644(54)	13.0(1.5)	38.5(5.4)					

sink and the inserted operator increases and (ii) as the mass gap, $M_{\text{excited}} - M_0$, increases. First, one can increase t_{sep}. Unfortunately, the signal also decreases exponentially as t_{sep} is increased so one is forced to compromise. In fact, the values of t_{sep} we have used reflect this compromise based on the anticipated statistics on each ensemble. Additionally, one can include excited states in the analysis of Eq. (2) as discussed below.

We include one excited state in the analysis of the two- and three-point functions. For operator insertion at zero momentum, the data are fit using the ansatzë

$$C^{\text{2pt}}(t_f, t_i) = |\mathcal{A}_0|^2 e^{-M_0(t_f - t_i)} + |\mathcal{A}_1|^2 e^{-M_1(t_f - t_i)}, \tag{10}$$

$$\begin{aligned} C^{\text{3pt}}_{\Gamma}(t_f, \tau, t_i) &= |\mathcal{A}_0|^2 \langle 0|\mathcal{O}_\Gamma|0\rangle e^{-M_0(t_f - t_i)} \\ &+ |\mathcal{A}_1|^2 \langle 1|\mathcal{O}_\Gamma|1\rangle e^{-M_1(t_f - t_i)} \\ &+ \mathcal{A}_0 \mathcal{A}_1^* \langle 0|\mathcal{O}_\Gamma|1\rangle e^{-M_0(\tau - t_i)} e^{-M_1(t_f - \tau)} \\ &+ \mathcal{A}_0^* \mathcal{A}_1 \langle 1|\mathcal{O}_\Gamma|0\rangle e^{-M_1(\tau - t_i)} e^{-M_0(t_f - \tau)}, \end{aligned} \tag{11}$$

where the source positions are shifted to $t_i = 0$ and $t_f = t_{\text{sep}}$. The states $|0\rangle$ and $|1\rangle$ represent the ground and "first" excited nucleon states, respectively. The four parameters, M_0, M_1, $\mathcal{A}_0$ and $\mathcal{A}_1$ are estimated first from the two-point function data. We find that the extraction of M_0 and $\mathcal{A}_0$ is stable under change of the fit range, while that of M_1 and $\mathcal{A}_1$ is not. We, therefore, choose the largest range, requiring that the values of, and the errors in, all four parameters do not jump by a large amount on changing the fit range. In all these fits, we find $M_1 \approx 2M_0$, so it should be considered an effective excited state mass as it is much larger than the $N(1440)$ excitation. The results of these best fits are given in Table IV.

We performed two independent measurements of the two-point functions, and the corresponding M_0, M_1, $\mathcal{A}_0$ and $\mathcal{A}_1$ are given in Table IV. The second set of measurements were obtained during the calculation of the disconnected diagrams using the AMA error reduction method discussed in Sec. IV A. We find that the two estimates are consistent within errors indicating no remaining bias with our choice of parameters for the AMA.

Fits using the ansatz for the three-point function given in Eq. (11) are used to isolate the two unwanted matrix elements $\langle 0|\mathcal{O}_\Gamma|1\rangle$ and $\langle 1|\mathcal{O}_\Gamma|1\rangle$. We find that the magnitude of $\langle 0|\mathcal{O}_\Gamma|1\rangle$ is about 16% of $\langle 0|\mathcal{O}_\Gamma|0\rangle$ and is determined with about 20% uncertainty on all the ensembles, whereas $|\langle 1|\mathcal{O}_\Gamma|1\rangle| \sim \langle 0|\mathcal{O}_\Gamma|0\rangle$, but has $O(100\%)$ errors. Ideally, equally precise data should be generated at each value of t_{sep}. In our analysis, however, the same number of measurements have been made for all t_{sep} on each ensemble, so errors increase with t_{sep} as shown in Fig. 2.

We reduce the contamination from higher excited states in these fits to the two- and three-point functions by excluding data points overlapping with, and adjacent to, the source and sink time slices at which the excited state contamination is the largest. For uniformity, we exclude 2, 3, 4 time slices on either end of the interval t_{src} to $t_{\text{src}} + t_{\text{sep}}$ in the three-point function for the $a = 0.12$, $a = 0.09$ and $a = 0.06$ fm ensembles, respectively. In physical units, these excluded regions correspond to roughly the same distance. This range of excluded points is consistent with the starting time slice of the fits to the two-point correlators given in Table IV, i.e., the time beyond which a two-state fit captures the two-point function data. Changing the exclusion time slice values to 3, 4, and 6 in both the fits changed the final estimates of the charges by less than 1σ.

Including a second exited state in the analysis would increase the number of matrix elements to be estimated from the three-point function by three. Given that their contribution would be smaller still, much higher statistics than generated for this study would be needed. This is confirmed in practice; the data are well fit with just the one excited state ansatz and there is no sensitivity left to resolve three additional small

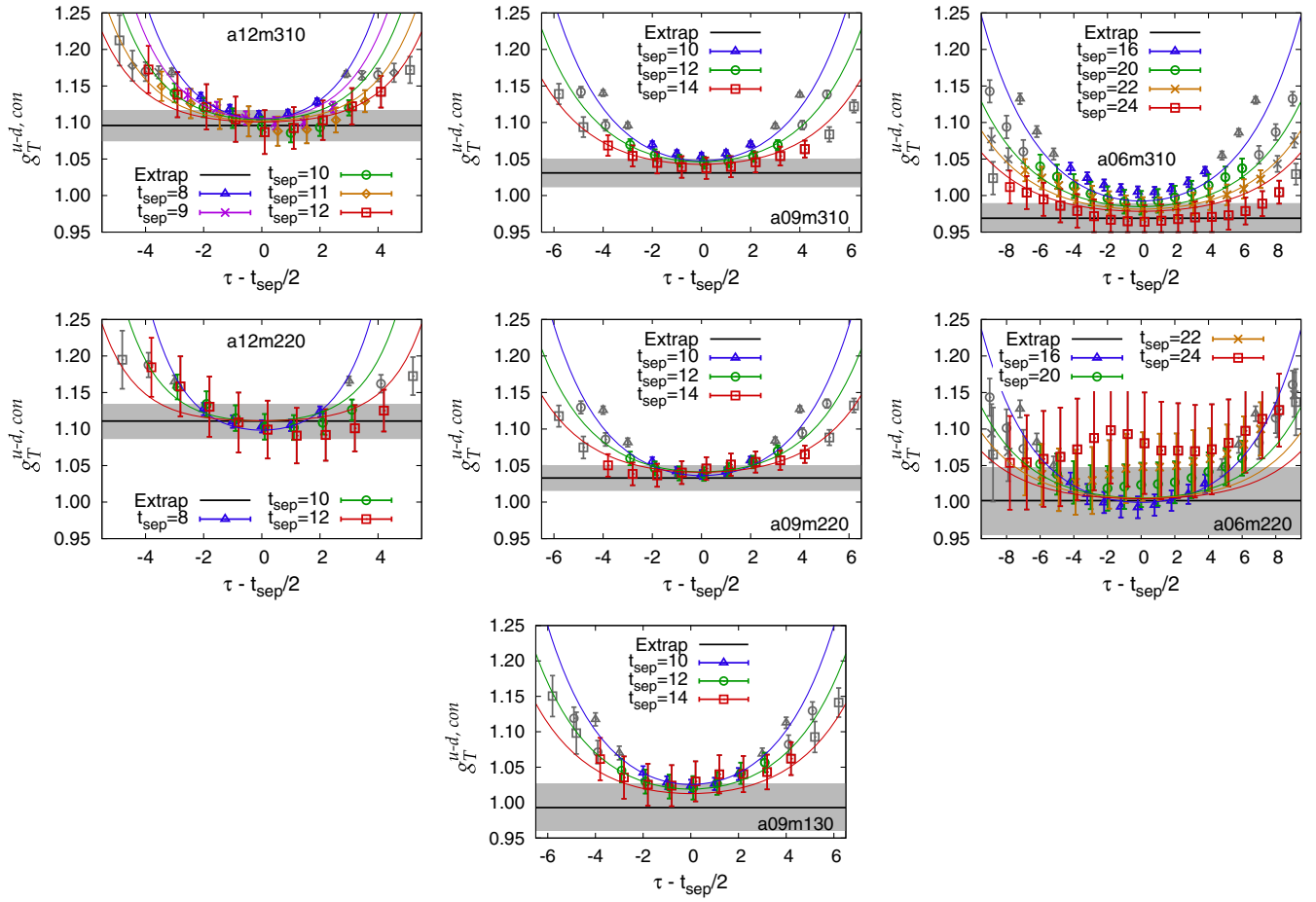

FIG. 2 (color online). The data for g_T^{u-d} and the results of the simultaneous fit using multiple $t_{\rm sep}$ using the ansatz given in Eq. (11) to isolate the excited state contribution. The seven figures are arranged as follows: the $M_\pi \approx 310$ MeV ensembles (top), $M_\pi \approx 220$ MeV ensembles (middle) and the $M_\pi \approx 130$ MeV ensemble (bottom). The solid black line and the grey band are the ground state ($t_{\rm sep} \to \infty$) estimate and error. The fits evaluated for different $t_{\rm sep}$ are also shown.

parameters. This analysis, using the ansatzë given in Eq. (11) and fitting the data at all $t_{\rm sep}$ simultaneously, was called the *two-simRR* method in Ref. [10].

Our overall conclusion is that, using the values of $t_{\rm sep}$ and the statistics for each ensemble given in Table III, and assuming that only one excited state gives a significant contribution, we are able to isolate and remove this contamination as illustrated in Fig. 2. It turns out that on all nine ensembles, the excited state contamination for g_T is small. It is worth remarking that this is not the case for g_A as discussed in [18].

D. Renormalization of operators

The calculation of the renormalization constants Z_Γ of the quark bilinear operators in the RI-sMOM scheme [19,20] has been done on five ensembles: *a12m310*, *a13m220*, *a09m310*, *a09m220* and *a06m310*. In order to translate the lattice results to the continuum $\overline{\rm MS}$ scheme at a fixed scale, say $\mu = 2$ GeV, used by phenomenologists we follow the procedure described in Ref. [10]. To summarize, the RI-sMOM estimate obtained at a given lattice four-momentum q^2 is first converted to the $\overline{\rm MS}$ scheme at the same scale (horizontal matching) using the one-loop perturbative matching. This value is then run in the continuum in the $\overline{\rm MS}$ scheme to the fixed scale, 2 GeV, using the two-loop anomalous dimension.

Ideally, one would like to establish a window $\Lambda \ll q \ll c/a$ in the RI-sMOM scheme in which the Z_Γ scales according to perturbation theory. Here Λ is an infrared scale below which nonperturbative effects are large and c/a represents the cutoff scale beyond which lattice discretization effects are large. The value of c is *a priori* unknown and the expectation is that it is $O(1)$. Within this window, the scaling of Z_T with q^2 gets contributions from both the anomalous dimension of the operator and the running of the strong coupling constant α_s. If this scaling is consistent with that predicted by perturbation theory, then estimates within this window would converge to a constant value independent of q^2 after conversion to $\overline{\rm MS}$ scheme and run

to a fixed scale, 2 GeV. As discussed in [10], HYP smearing the lattice to reduce the ultraviolet noise in the measurements also reduces the upper cutoff c/a for the calculation of the renormalization constants, and *a priori*, we again do not know by how much smearing shrinks the desired window or whether it totally eliminates it on the various 0.06–0.12 fm lattices we have analyzed. Below we summarize the tests performed and state the results.

(i) We first test the data for the Z's in the RI-sMOM scheme to see if they exhibit the desired perturbative behavior for HYP smeared lattices by calculating the logarithmic derivative of $Z(q^2)$ and comparing it to the anomalous dimension. The data show evidence of such a window in the calculation of the vector, axial and tensor renormalization constants, but not for the scalar. In this paper, we only need Z_T and Z_V, so we next describe how we obtained final estimates for these and assigned a conservative error that covers the various sources of systematic uncertainties.

(ii) We find that the ratios of renormalization constants, Z_Γ/Z_V, have less fluctuations and are flatter in q^2 as illustrated in Fig. 3. This improvement is presumably due to the cancellation of some of the systematic uncertainties in the ratio, including, for example, those due to the breaking of the continuum Lorentz symmetry to the hypercubic rotation group on the lattice that impacts the calculation of the Z-factors. On each ensemble, the final renormalized charges can be constructed from these ratios as $(Z_\Gamma/Z_V)\times(g_\Gamma/g_V^{u-d})$ using the identity $Z_V g_V^{u-d}=1$. Because of the better signal and resulting fits, we use the estimates from the ratios method for our central values and include the difference between these and estimates from the direct calculation, $Z_\Gamma g_\Gamma$, as an estimate of the systematic error.

(iii) To take into account the remaining dependence on q^2 of the estimates in the $\overline{\text{MS}}$ scheme at 2 GeV, we carry out the two analysis strategies proposed in Ref. [10]. In the first, we obtain the value and error from the fit to the data using the ansatz $c/q^2+Z+\alpha q$. We find that these fits capture the data and the extrapolations $Z+\alpha q$ are shown as dashed lines in Fig. 3.

(iv) A slightly modified version of the second method is used: we now choose the q^2 in the RI-sMOM scheme by the condition $q_i a-\sin(q_i a)=0.05$ based on bounding the discretization error and the error in Z is estimated from the spread in the data over a range in q^2 about this point. This choice corresponds to $q^2=5$, 9 and 21 GeV^2 for the $a=0.12$, 0.09 and 0.06 fm ensembles, respectively. The corresponding ranges for determining the error were taken to be 4–6, 8–10 and 18–24 GeV^2 over which the data show a reasonably flat behavior as shown in Fig. 3.

(v) For the final estimates we take the average of the two methods. The error is taken to be half the difference, and rounded up to be conservative.

(vi) On the ensembles at the two lattice spacings $a=0.12$ and 0.09 fm, we found no significant difference in the estimates of the renormalization constants for the two different quark masses ($M_\pi=310$ and 220 MeV ensembles). A common fit captured both data sets, as shown in Fig. 3, and was used to extract our "quark mass independent" estimates.

(vii) The entire calculation, matching to the $\overline{\text{MS}}$ scheme, running to 2 GeV and the final fits for the two strategies, was done using 200 bootstrap samples because the number of configurations analyzed in ensembles *a12m310* and *a12m220* (*a09m310* and *a09m220*) are different.

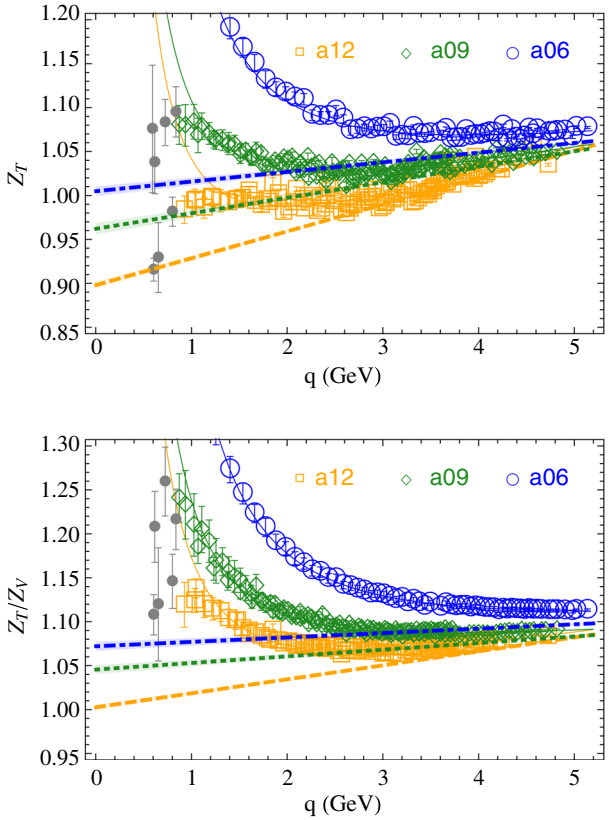

FIG. 3 (color online). Data for Z_T (upper) and Z_T/Z_V (lower) after translation to the $\overline{\text{MS}}$ scheme at 2 GeV as a function of the lattice momentum q. The lattice calculation was done on five ensembles in the RI-sMOM scheme. The $a=0.12$ fm ($a=0.09$ fm) fit are to the combination of *a12m310* and *a12m220* (*a12m310* and *a12m220*) data as there is no detectable dependence on the quark mass. The $a=0.06$ fm fit is to the *a06m310* ensemble data. The data were fit using the ansatz $c/q^2+Z+\alpha q$ and the dashed lines show the extrapolation $Z+\alpha q$.

TABLE V. The mass independent renormalization constants Z_T, Z_V and the ratio Z_T/Z_V in the $\overline{\text{MS}}$ scheme at 2 GeV at the three values of the lattice spacings used in our calculations. These estimates are obtained using the fit $1/q^2 + Z + \alpha q$ (left) and as an average over an interval in q^2 (middle) as described in the text. For the final estimates, shown in the last 3 columns, we take the average of the two methods and half the difference (rounded up) for the errors.

ID	Z_T	Z_V	Z_T/Z_V	Z_T	Z_V	Z_T/Z_V	Z_T	Z_V	Z_T/Z_V
a12	0.898(4)	0.890(4)	1.003(3)	0.995(10)	0.918(12)	1.073(2)	0.95(5)	0.90(2)	1.04(4)
a09	0.962(6)	0.911(9)	1.045(5)	1.026(6)	0.938(6)	1.089(2)	0.99(4)	0.925(15)	1.07(3)
a06	1.005(6)	0.931(4)	1.072(5)	1.071(5)	0.961(5)	1.1134(6)	1.04(4)	0.945(15)	1.09(3)

The final mass-independent renormalization constants at the three lattice spacings needed to construct the renormalized charges in the two ways: (i) $Z_\Gamma g_\Gamma$ and (ii) from the product of the ratios $(Z_\Gamma/Z_V) \times (g_\Gamma/g_V^{u-d})$ with the identity $Z_V g_V^{u-d} = 1$ are given in Table V. The errors in the renormalization factors, Z_T and Z_T/Z_V, are added in quadratures to those in the extraction of the bare nucleon charges g_T^{bare} and $g_T^{\text{bare}}/g_V^{\text{bare}}$, respectively, to get the final estimates of the renormalized charges given in Table VII.

E. Statistical analysis of two-point and three-point functions

We carried out the following statistical analyses of the data on each ensemble to look for anomalies. We divided the data for a given ensemble into bins of about 1000 measurements (by source points and by configuration generation order) to test whether the ensembles consist of enough independent configurations. For bin sizes >5 configurations, the errors in the mean decreased as $\sqrt{N}$, i.e., consistent with our analysis of the autocorrelation coefficient of about 5 configurations (about 25 molecular dynamics steps). Also, the error computed with data averaged over S source points on each configuration is smaller by $\sqrt{S}$ compared to the error in the data from any one of the source position.

Estimates from bins of about 1000 measurements, however, fluctuated by up to 3σ in some cases. This variation is much larger than expected based on the bin sizes. To determine whether the data in the various bins satisfy the condition of being drawn from the same distribution, we performed the Kolmogorov-Smirnov (K-S) test on quantities that have reasonable estimates configuration by configuration, for example, the isovector vector charge g_V^{u-d} and the value of the two-point function at a given time separation. The K-S test showed acceptable probability of the various bins being drawn from the same distribution. Histograms of the data showed no long tails in the distribution but exhibit variations in the sample distribution that becomes increasingly Gaussian as the bin size was increased to the full sample size.

We find these 2–3σ fluctuations both when the data are binned by the source position and when the configurations are divided into two halves according to the molecular dynamics generation order. Such fluctuations are apparent in the *a06m310* and the *a06m220* ensemble data. Comparing the data for different charges (axial, scalar and tensor), we found that the effect is least significant (less than 1σ) for the tensor charge and worst for the vector charge g_V; it is, presumably, most evident in g_V because it has the smallest statistical errors. We offer two possible explanations. One, the large variation observed in the bin mean indicates that the ensembles of $O(1000)$ configurations (spanning a total of 5000-6000 molecular dynamics evolution steps in the generation of thermalized HISQ lattices we have used) have not covered enough phase space and bin errors are consequently underestimated. The other explanation is that, since we used the same four or eight source positions on all configurations in an ensemble, the data for fixed source position is more correlated. Our ongoing tests confirm that using random but well-separated source positions on each configuration is a better strategy. Finally, based on the convergence of the bin distributions to a Gaussian on increasing the bin size to the full sample and the lack of evidence of long tails, makes us confident that the final error estimates are reliable.

Our overall conclusion about statistics is that while $O(10,000)$ measurements on these ensembles of $O(1000)$ configurations are sufficient for extracting the tensor charge with few percent uncertainty, one will need a factor of ten or more in statistics for obtaining the scalar charge with similar accuracy. This goal is currently being pursued using the AMA method discussed in Sec. IV.

Lastly, we performed both correlated and uncorrelated fits to the nucleon two-point function data. In all cases in which the correlated fits were stable under changes in the fit ranges and had reasonable χ^2, the two fits gave overlapping estimates. Since correlated fits did not work in all cases, all statistical errors in the two- and three-point correlation functions were, thereafter, calculated using a single elimination jackknife method with uncorrelated fits performed on each jackknife sample.

III. CONTRIBUTION OF THE CONNECTED DIAGRAM

Estimates of the bare and renormalized charges on the nine ensembles at different lattice spacings, light quark masses and lattice volumes are given in Tables VI and VII.

To extrapolate these estimates to the physical point, i.e., the continuum limit ($a \to 0$), the physical pion mass ($M_{\pi^0} = 135$ MeV) and the infinite volume limit ($L \to \infty$), we explored the four parameter ansatz

$$g_T^i = c_1^i \left[1 + \frac{M_\pi^2}{(4\pi F_\pi)^2} f^i\left(\frac{M_\pi}{\mu}\right)\right] + c_2^i a + c_3^i(\mu) M_\pi^2 + c_4^i e^{-M_\pi L}, \quad (12)$$

where we have included the leading chiral logarithms [21]. The loop functions $f^i(\mu/M_\pi)$ for the two isospin channels are

$$f^{u+d} = \frac{3}{4}\left[(2 + 4g_A^2)\log\frac{\mu^2}{M_\pi^2} + 2 + g_A^2\right] = 2.72 + 6.38\log\frac{\mu^2}{M_\pi^2}, \quad (13)$$

$$f^{u-d} = \frac{1}{4}\left[(2 + 8g_A^2)\log\frac{\mu^2}{M_\pi^2} + 2 + 3g_A^2\right] = 1.72 + 3.75\log\frac{\mu^2}{M_\pi^2}, \quad (14)$$

where we use $\mu = M_\rho = 770$ MeV for the renormalization scale and $g_A = 1.276$. The extrapolation ansatz is taken to be linear in a because the discretization errors in the clover-on-HISQ formalism with unimproved operators start at $\mathcal{O}(a)$. Similarly, we have kept only the leading finite volume correction term, $e^{-M_\pi L}$. In Fig. 4, we compare the fit obtained using Eq. (12) with that using the simpler isospin independent four parameter ansatz without the chiral logarithm:

$$g_T(a, M_\pi, L) = c_1 + c_2 a + c_3 M_\pi^2 + c_4 e^{-M_\pi L}. \quad (15)$$

Both fits have reasonable χ^2/dof and the estimates at the physical point are consistent. The fit including the chiral logarithm would naively indicate that g_T should decrease in value with increasing M_π^2 for $M_\pi > 300$ MeV. Such a behavior is not seen in the global data shown in Fig. 12. We conclude that the large curvature due to the chiral logarithm seen in Fig. 4 is most likely due to the number and accuracy of the data and of keeping just the leading chiral correction. Also, the error estimate from the fit using the simpler ansatz given in Eq. (15) is more conservative and covers the full range of both fits. We, therefore, use Eq. (15) for all further analyses in this paper.

TABLE VI. The bare connected ($g_T^{\rm con}$) and disconnected ($g_T^{\rm disc}$) contributions to the tensor charges of the proton on the nine ensembles. Dots indicate that those ensembles have not been simulated. The isovector vector charge g_V^{u-d} is used to construct ratios for noise reduction as described in the text.

ID	$g_T^{{\rm con},u}$	$g_T^{{\rm con},d}$	$g_T^{{\rm con},u-d}$	$g_T^{{\rm con},u+d}$	$g_T^{{\rm disc},l}$	$g_T^{{\rm disc},s}$	$g_V^{{\rm con},u-d}$
a12m310	0.875(18)	−0.2208(93)	1.096(21)	0.655(20)	−0.0124(23)	−0.0041(20)	1.069(9)
a12m220S	0.873(26)	−0.212(17)	1.086(26)	0.661(36)	⋯	⋯	1.059(12)
a12m220	0.888(22)	−0.222(12)	1.111(24)	0.665(26)	−0.0038(41)	−0.0010(28)	1.074(11)
a12m220L	0.859(18)	−0.198(10)	1.058(19)	0.662(21)	⋯	⋯	1.065(7)
a09m310	0.829(16)	−0.2025(80)	1.031(19)	0.626(18)	−0.0050(21)	−0.0005(21)	1.056(8)
a09m220	0.820(16)	−0.2120(79)	1.033(17)	0.608(18)	⋯	−0.0021(53)	1.050(9)
a09m130	0.779(33)	−0.214(18)	0.993(33)	0.565(42)	⋯	⋯	1.029(16)
a06m310	0.778(18)	−0.1898(86)	0.969(20)	0.588(21)	−.0035(62)	−0.0005(52)	1.040(8)
a06m220	0.759(43)	−0.241(19)	1.002(46)	0.519(48)	⋯	⋯	0.993(18)

TABLE VII. The renormalized connected (g_T) and disconnected ($g_T^{\rm disc}$) contributions to the tensor charges of the proton on the nine ensembles. The errors are obtained by adding in quadratures the statistical errors given in Table VI in the bare charges to the errors in the renormalization constants given in Table V.

ID	$g_T^{{\rm con},u}$	$g_T^{{\rm con},d}$	$g_T^{{\rm con},u-d}$	$g_T^{{\rm con},u+d}$	$g_T^{{\rm disc},l}$	$g_T^{{\rm disc},s}$
a12m310	0.852(37)	−0.215(12)	1.066(46)	0.637(31)	−0.0121(23)	−0.0040(19)
a12m220S	0.857(43)	−0.209(19)	1.066(50)	0.649(44)	⋯	⋯
a12m220	0.860(40)	−0.215(15)	1.075(48)	0.644(36)	−0.0037(40)	−0.0010(27)
a12m220L	0.840(37)	−0.194(12)	1.033(45)	0.647(33)	⋯	⋯
a09m310	0.840(28)	−0.2051(98)	1.045(34)	0.634(25)	−0.0050(22)	−0.0005(21)
a09m220	0.836(28)	−0.216(10)	1.053(34)	0.619(25)	⋯	−0.0021(54)
a09m130	0.809(40)	−0.222(20)	1.032(44)	0.587(45)	⋯	⋯
a06m310	0.815(29)	−0.199(10)	1.015(34)	0.617(27)	−0.0037(65)	−0.0005(55)
a06m220	0.833(52)	−0.264(22)	1.099(59)	0.569(55)	⋯	⋯

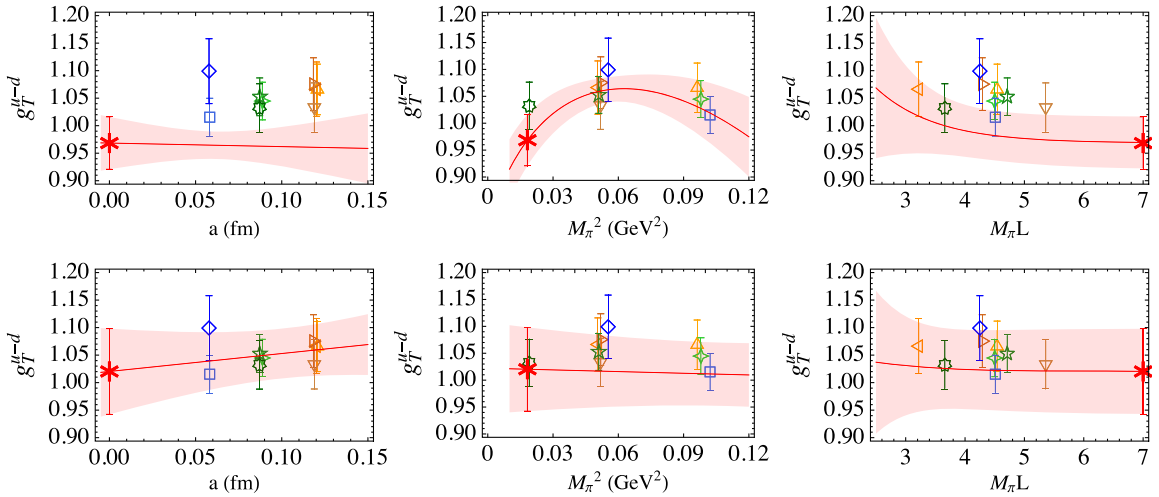

FIG. 4 (color online). Comparision of the simultaneous fits versus a, M_π^2 and $M_\pi L$ to the iso-vector charge, g_T^{u-d}, data using Eq. (12) (top) with the simpler version without the chiral logarithms given in Eq. (15) (bottom). The data symbols are defined in Table I. The fit is given by the red line and the physical value after extrapolation to the continuum limit ($a \to 0$), physical pion mass ($M_\pi \to M_{\pi^0}^{\rm phys}$) and infinite volume ($L \to \infty$) is marked by a red star. The error band is shown as a function of each variable holding the other two at their physical value. The data are shown projected on to each of the three planes.

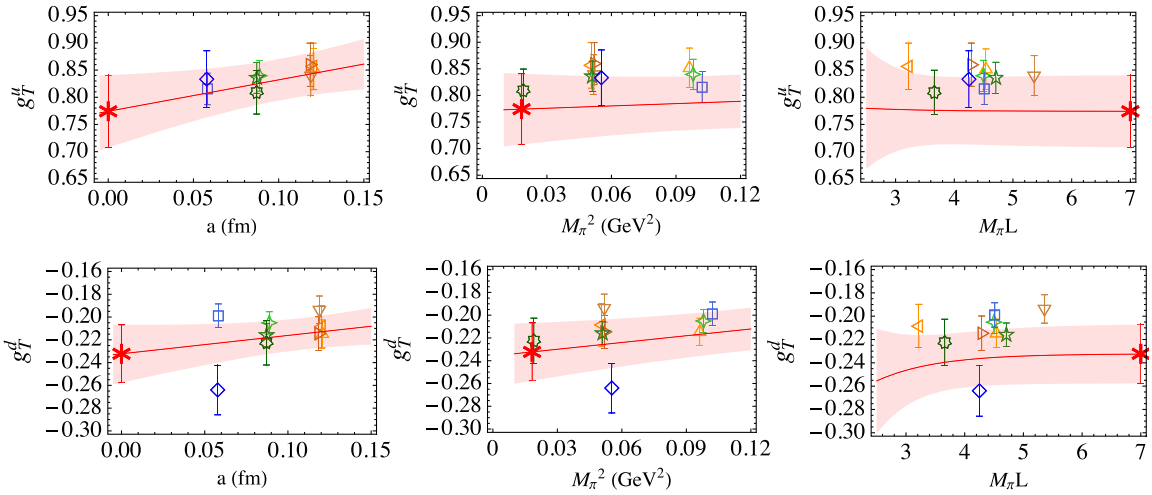

FIG. 5 (color online). Simultaneous extrapolation to the physical point ($a \to 0$, $M_\pi \to M_{\pi^0}^{\rm phys}$, and $L \to \infty$) using Eq. (15), of the connected contributions to the flavor diagonal nucleon (proton) tensor charges, g_T^u (upper) and g_T^d (lower), renormalized in the $\overline{\rm MS}$ scheme at 2 GeV. The physical values given by the fit are marked by a red star. The rest is the same as in Fig. 4.

The results of the fits using Eq. (15) and the extrapolated value are shown in Fig. 5 separately for operator insertion on the u and d quarks in the nucleon. We find that the g_T^u contribution is larger and essentially flat in all three variables (lattice spacing, pion mass and volume), while the g_T^d connected contribution is much smaller and shows a slightly larger relative spread. The spread in g_T^d on the $a = 0.06$ fm lattices is an example of the unexpectedly large statistical fluctuations we mentioned in Sec. II E that will require higher statistics to resolve. The final renormalized extrapolated values for the proton charges are

$$g_T^u(\text{con}) = 0.774(65),$$
$$g_T^d(\text{con}) = -0.233(25). \quad (16)$$

The χ^2/dof is 0.1 and 1.6 for g_T^u and g_T^d, respectively, with dof = 5. In performing the fits, we assume that the error in each data point has a Gaussian distribution even though the quoted 1σ error is a combination of the statistical error and the systematic error coming from the calculation of the renormalization factor Z_T. The fits to the isovector $g_T^u - g_T^d$ and the connected part of the isoscalar $g_T^u + g_T^d$ data using Eq. (15), are shown in Fig. 6. Our final estimates are

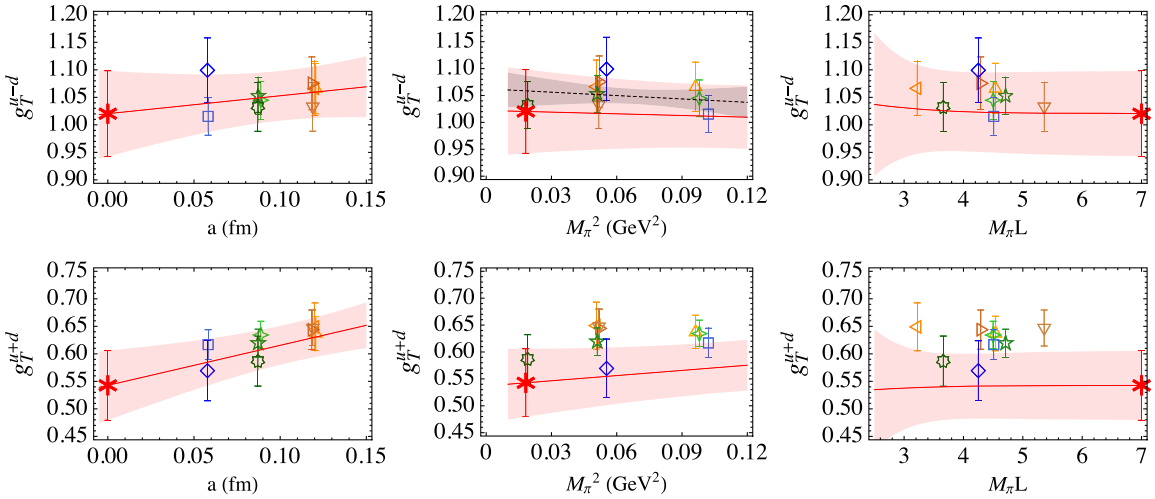

FIG. 6 (color online). Simultaneous extrapolation to the physical point ($a \to 0$, $M_\pi \to M_{\pi^0}^{\rm phys}$, and $L \to \infty$) using Eq. (15) of the connected contributions to the isovector g_T^{u-d} (upper) and isoscalar g_T^{u+d} (lower) nucleon (proton) tensor charges renormalized in the $\overline{\rm MS}$ scheme at 2 GeV. The overlay in the middle upper figure, with the dashed line within the thin gray band, is the fit to the data versus M_π^2 assuming no dependence on the other two variables. Rest is the same as in Fig. 4.

$$g_T^{u-d}({\rm con}) = 1.020(76),$$
$$g_T^{u+d}({\rm con}) = 0.541(62). \tag{17}$$

with a $\chi^2/{\rm dof} = 0.4$ and 0.2, respectively.

IV. CONTRIBUTION OF THE DISCONNECTED DIAGRAM

In Sec. II B we showed that to estimate the disconnected contribution, we need to calculate two quantities at zero-momentum—the nucleon two-point function and the contraction of the bilinear fermion operator into a quark loop—and measure their correlation. These two calculations are described below.

A. Two-point function

The high statistics calculation of the two-point function with smeared sources was redone using the all-mode-averaging (AMA) technique [17] because quark propagators from the earlier connected three-point function study were too expensive to store. To implement AMA, we again choose four different source time slices separated by $L_T/4$ on each configuration. On each of these time slices we calculate the two-point correlator by placing $N_{\rm LP} = 15$ low precision (LP) sources, for a total of $4 \times 15 = 60$ sources per configuration. This estimate is *a priori* biased due to the LP calculation. In addition, on each of these four time slices we place one high precision (HP) source, i.e., $N_{\rm HP} = 4$ such sources per configuration, from which we calculate a LP and a HP correlator. These four HP and LP correlators are used to correct the bias in the 60 LP estimates, i.e., on each configuration, the two-point function is given by

$$C^{\rm 2pt,imp}(t,t_0) = \frac{1}{N_{\rm LP}}\sum_{i=1}^{N_{\rm LP}} C_{\rm LP}^{\rm 2pt}(t;t_0,\mathbf{x}_i^{\rm LP}) + \frac{1}{N_{\rm HP}}\sum_{i=1}^{N_{\rm HP}}[C_{\rm HP}^{\rm 2pt}(t;t_0,\mathbf{x}_i^{\rm HP}) - C_{\rm LP}^{\rm 2pt}(t;t_0,\mathbf{x}_i^{\rm HP})], \tag{18}$$

where $C_{\rm LP}^{\rm 2pt}$ and $C_{\rm HP}^{\rm 2pt}$ are the two-point correlation function calculated in LP and HP, respectively, and $\mathbf{x}_i^{\rm LP}$ and $\mathbf{x}_i^{\rm HP}$ are the two kinds of source positions.

The basic idea of AMA is that, in the low-precision evaluation, the LP average [first term in Eq. (18)] is biased, and this bias depends predominately on low modes of the Dirac operator that are independent of the source position and can be corrected by the second term. Thus, we get an unbiased estimate from 60 LP source points for the computational cost of $(60 + 4)$ LP and 4 HP calculations. In our current implementation, 15 LP measurements cost the same as one HP when using the multigrid algorithm for inverting the Dirac matrix [22]. [On the *a06m310* ensemble we used $(92 + 4)$ LP and 4 HP sources and the errors decreased by a factor of $\sim$1.2 compared to $(60 + 4)$ LP sources.] Comparing the errors in the estimates for masses given in Table IV, we find that the AMA errors are a factor of 2–4 times smaller than those from the connected study (all HP measurements). Since this improvement is based on comparing 120 LP (we effectively doubled the LP statistics by analyzing both the forward and backward propagation of the nucleon) versus 8 HP measurements, we conclude that the correlations between the 120 LP measurements on each configuration are small.

If we assume that the variance of both the LP and HP measurements is the same and given by σ and the

correlation between the HP and LP measurements from the $N_{\rm HP}$ points, $\mathcal{C} = \sigma^2_{\rm NP,LP}/\sigma^2$, is small, then the statistical error in Eq. (18) is given by [17]

$$\sigma^{\rm imp} \approx \sigma\sqrt{\frac{1}{N_{\rm LP}} + \frac{2}{N_{\rm HP}}(1-\mathcal{C})}. \tag{19}$$

The second term in the square root becomes smaller as the LP estimate approaches the HP estimate and the correlation factor $\mathcal{C} \to 1$. By controlling $N_{\rm LP}$, $N_{\rm HP}$ and $\mathcal{C}$, we can minimize the total error for a fixed computational cost.

To speed up the AMA method we exploit the fact that the same Dirac matrix is inverted multiple times[1] on each configuration. It is, therefore, efficient to precondition the matrix by deflating the low-eigenmodes. We implement such improvement using the multigrid solver [22,23] which has deflation built in. To obtain the LP estimate of the two-point function, we truncate the multigrid solver using a low-accuracy stopping criterion: the ratio ($r_{\rm LP} \equiv |\text{residue}|_{\rm LP}/|\text{source}|$) is chosen to be 10^{-3} for all the ensembles. Our final analysis of the masses, amplitudes and matrix elements, however, shows that this stopping criteria was overly conservative as the bias correction term is negligible compared to the statistical errors.

B. Disconnected quark loop

For the evaluation of the quark loop term $\sum_{\mathbf{x}} {\rm Tr}[M^{-1}(\tau,\mathbf{x};\tau,\mathbf{x})\Gamma]$, we adopt the stochastic method accelerated with a combination of the truncated solver method (TSM) [15,16], the hopping parameter expansion (HPE) [24,25] and the dilution technique [26–28]. To obtain a stochastic estimate of the quark loops, consider a set of random complex noise vectors $|\eta_i\rangle$ for $i = 1, 2, 3, \ldots, N$, having color, spin and spacetime components with the following properties:

$$\frac{1}{N}\sum_{i=1}^{N} |\eta_i\rangle = \mathcal{O}\left(\frac{1}{\sqrt{N}}\right), \tag{20}$$

$$\frac{1}{N}\sum_{i=1}^{N} |\eta_i\rangle\langle\eta_i| = \mathbb{1} + \mathcal{O}\left(\frac{1}{\sqrt{N}}\right). \tag{21}$$

We choose complex Gaussian noise vectors, i.e., we fill all the spin, color and spacetime components of the vector with $(r_r + i r_i)/\sqrt{2}$, where r_r and r_i are Gaussian random numbers, because they give marginally smaller statistical error than $\mathbb{Z}_N$ random noise when combined with the HPE.

These random vectors are used as sources for the inversion of the Dirac matrix. Then, from the solutions $|s_i\rangle$ of the Dirac equation,

$$M|s_i\rangle = |\eta_i\rangle, \tag{22}$$

the inverse of the Dirac matrix is given by

$$M^{-1} = \frac{1}{N}\sum_{i=1}^{N} |s_i\rangle\langle\eta_i| + M^{-1}\left(\mathbb{1} - \frac{1}{N}\sum_{i=1}^{N} |\eta_i\rangle\langle\eta_i|\right) \tag{23}$$

$$= \frac{1}{N}\sum_{i=1}^{N} |s_i\rangle\langle\eta_i| + \mathcal{O}\left(\frac{1}{\sqrt{N}}\right). \tag{24}$$

The stochastic estimate of the zero-momentum insertion of the operator contracted into a quark loop is then given by

$$\sum_{\mathbf{x}} {\rm Tr}[M^{-1}(\tau,\mathbf{x};\tau,\mathbf{x})\Gamma] \approx \frac{1}{N}\sum_{i=1}^{N} \langle\eta_i|_\tau \Gamma |s_i\rangle_\tau, \tag{25}$$

where $|\eta\rangle_\tau$ is a vector whose $t = \tau$ components are filled with random numbers, and the entries on other time slices are set to zero.

In the estimation of the inverse of the Dirac matrix by using random sources, Eq. (24), one can use the mixed-precision technique called the truncated solver method (TSM) [15,16]. The idea of the TSM is the same as the AMA used in the evaluation of the two-point function. Consider two kinds of solution vectors of Eq. (22) for a given random source $|\eta_i\rangle$ with different precision: $|s_i\rangle_{\rm LP}$ and $|s_i\rangle_{\rm HP}$, where $|s_i\rangle_{\rm LP}$ is the low precision computationally cheap estimate of the solution, while $|s_i\rangle_{\rm HP}$ is the high precision solution. The low precision estimate, $|s_i\rangle_{\rm LP}$, was obtained by truncating the multigrid inverter at $r_{\rm LP} = 5 \times 10^{-3}$. The bias with this choice of $r_{\rm LP}$ will be discussed later in this section.

By using the LP and HP solutions, the unbiased estimator of M^{-1} is again given by

$$M_E^{-1} = \frac{1}{N_{\rm LP}}\sum_{i=1}^{N_{\rm LP}} |s_i\rangle_{\rm LP}\langle\eta_i| + \frac{1}{N_{\rm HP}}\sum_{i=N_{\rm LP}+1}^{N_{\rm LP}+N_{\rm HP}} (|s_i\rangle_{\rm HP} - |s_i\rangle_{\rm LP})\langle\eta_i|. \tag{26}$$

The first term in the right-hand-side (r.h.s) is the LP estimate of M^{-1} while the second term in the r.h.s corrects the bias. As described in the case of the two-point function estimation, the total statistical error of M_E^{-1} scales as Eq. (19). In other words, there are again two sources of statistical error in M_E^{-1}: one is the LP estimate that scales as $\sqrt{1/N_{\rm LP}}$, and the other is the correction term that scales as $\sqrt{1/N_{\rm HP}}$. The size of the statistical error in the correction term is determined by the correlation between $|s_i\rangle_{\rm HP}$ and $|s_i\rangle_{\rm LP}$.

In the TSM, there are three parameters we can tune to minimize the statistical error for a given computation cost:

[1]The number of inversions of the Dirac matrix per configuration are $12 \times (N_{\rm LP} + N_{\rm HP})$.

$N_{\rm LP}$, $N_{\rm LP}/N_{\rm HP}$ and the LP stopping criteria $r_{\rm LP}$. Note that once $N_{\rm LP}/N_{\rm HP}$ and $r_{\rm LP}$ are determined, the total error scales as $\sqrt{1/N_{\rm LP}}$. Hence $N_{\rm LP}$ determines the size of the error, and $N_{\rm LP}/N_{\rm HP}$ and $r_{\rm LP}$ determine the efficiency of the estimator in terms of the computational cost. To maximize the efficiency, we tune the $N_{\rm LP}/N_{\rm HP}$ and $r_{\rm LP}$ so that the size of the error from the correction term is much smaller as it minimizes the computation time. In this study, we use $N_{\rm LP}/N_{\rm HP} = 30$ or 50 (See Table. VIII) and $r_{\rm LP} \sim 5 \times 10^{-3}$. With this accuracy, we find that the bias correction term is $\sim$10% of the final estimate of $g_T^l(\mathrm{disc})$ and about half of the statistical error.

We improve the TSM by using the hopping parameter expansion (HPE) [24,25] as a preconditioner to reduce the statistical noise. In the HPE one writes the clover Dirac matrix as

$$M = \frac{1}{2\kappa}(\mathbb{1} - \kappa D), \tag{27}$$

where κ is the hopping parameter. The inverse can then be written as

$$\frac{1}{2\kappa}M^{-1} = \mathbb{1} + \sum_{i=1}^{n-1}(\kappa D)^i + (\kappa D)^n \frac{1}{2\kappa}M^{-1}. \tag{28}$$

By taking $n = 2$, the disconnected quark loop is given by

$$\mathrm{Tr}[M^{-1}\Gamma] = \mathrm{Tr}[(2\kappa\mathbb{1} + 2\kappa^2 D + \kappa^2 D^2 M^{-1})\Gamma]. \tag{29}$$

Here, the first two terms of the r.h.s do not contribute to the nucleon tensor charge because $\mathrm{Tr}\Gamma = \mathrm{Tr}(\Gamma\gamma_\mu) = 0$. As a result, the only nontrivial term that we need to calculate is $\mathrm{Tr}[\kappa^2 D^2 M^{-1}\Gamma]$. Because the two leading terms, which would otherwise contribute only to the noise, are removed from the stochastic estimation, HPE works as an error reduction technique. Tests using the *a12m310* ensemble show that the statistical error of the disconnected contribution to the tensor charge is reduced by a factor of about 2.5 with HPE.

As shown in Eq. (23), the noise in the stochastic estimation for M^{-1} is proportional to M^{-1}, whose magnitude decreases exponentially as the spacetime distance between source and sink increases. Hence it is possible to reduce the statistical noise by placing noise sources only on part of the whole time slice, choosing maximally separated points, and fill the other points on the time slice with zero. This procedure divides the time slice into m subspaces, and the answer for the full time slice is obtained by combining results of the m subspaces. The computational cost increases by a factor of m because Dirac inversions are needed for each noise source vector defining a subspace. Hence this technique is useful when the reduction in noise wins over the increase in computational cost. This is called the time dilution method [26–28]. Unfortunately, we find that the increase in computational cost is equal to or larger than the gain from the reduction of statistical noise for the nucleon charges. Hence we place random sources on all points of a time slice and for each time slice that we want to evaluate the operator on.

There is one more symmetry that can be used for noise reduction: γ_5-hermiticity of clover Dirac operator, $M^\dagger = \gamma_5 M \gamma_5$. Because of this symmetry, the quark loop for tensor channel should be pure imaginary, and the nucleon two-point function is real. Hence we set the real part of the quark loop to zero when constructing the correlation function and averaging over the configurations in Eq. (7).

To increase the statistics, we average over the three possible combinations of $\gamma_i\gamma_j$ and forward/backward propagators. The final values of $t_{\rm sep}$ investigated, the displacement τ with respect to the source time slice of the two-point correlator on which the operator was inserted, the statistics and the number of random noise sources used on each configuration are given in Table VIII.

C. Results for the disconnected contributions

The calculation of the disconnected diagram is computationally expensive so it has been done on only four ensembles: *a12m310*, *a12m220*, *a09m310* and *a06m310*.

TABLE VIII. The parameters used in the study of the disconnected diagrams. The source-sink time separations analyzed ($t_{\rm sep}$), the time slices (τ) on which the operator is inserted as explained in the text, the number of configurations analyzed ($N_{\rm conf}$) and the number of random noise sources ($N_{\rm LP}$) used on each configuration. Here $\{A \sim B\}$ denotes the set of consecutive integers from A to B. The number $N_{\rm LP}/N_{\rm HP}$ gives the ratio of the number of low to high precision calculations done. The LP criteria for stopping the Dirac matric inversion was set to $r_{\rm LP} = 0.005$. For the associated two-point function calculation, we used AMA with 64 LP and 4 HP measurements on each configuration and the results for the masses and amplitudes are given in Table IV.

ID	$t_{\rm sep}/a$	τ/a	$N_{\rm conf}^{{\rm disc},l}$	$N_{\rm conf}^{{\rm disc},s}$	$N_{\rm LP}^{{\rm disc},l}$	$N_{\rm LP}^{{\rm disc},s}$	$N_{\rm LP}/N_{\rm HP}$
a12m310	$\{8 \sim 14\}$	$3, 4, \ldots, 11$	1013	1013	5000	1500	30
a12m220	$\{8 \sim 14\}$	$3, 4, \ldots, 11$	958	958	11000	4000	30
a09m310	$\{10 \sim 16\}$	6, 7, 8, 9	1081	1081	4000	2000	30
a09m220	$\{10 \sim 16\}$	5, 6, 7, 8, 9	⋯	200	10000	8000	50
a06m310	$\{16 \sim 24\}$	$6, 8, 10, \ldots, 18$	100	200	10000	5000	50

These four ensembles provide an understanding of the discretization errors and of the behavior as a function of the quark mass. To get the full contribution of the quark EDM to the nucleon EDM, we also need to evaluate the disconnected diagram with a strange quark loop. Since the calculation with the strange quark are computationally cheaper, we have also analyzed a fifth ensemble, *a09m220*, for that estimate.

We use the fit ansatz given in Eq. (11), i.e., the same *two-state-fit* method used to fit the data for the connected three-point diagrams, to extract the ground state results for the disconnected contribution. The data and the results of the fit for the light and strange quark loop on the *a12m310* ensemble are shown in Figs. 7 and 8, respectively. We find significant contribution from excited states only on the *a12m310* ensemble for light quark disconnected diagram—it is large for $t_{\rm sep} = 8$, but by $t_{\rm sep} = 12$ the data agree with the final extrapolated value. The peculiar pattern seen in the *a06m310* ensemble is most likely due to the small number

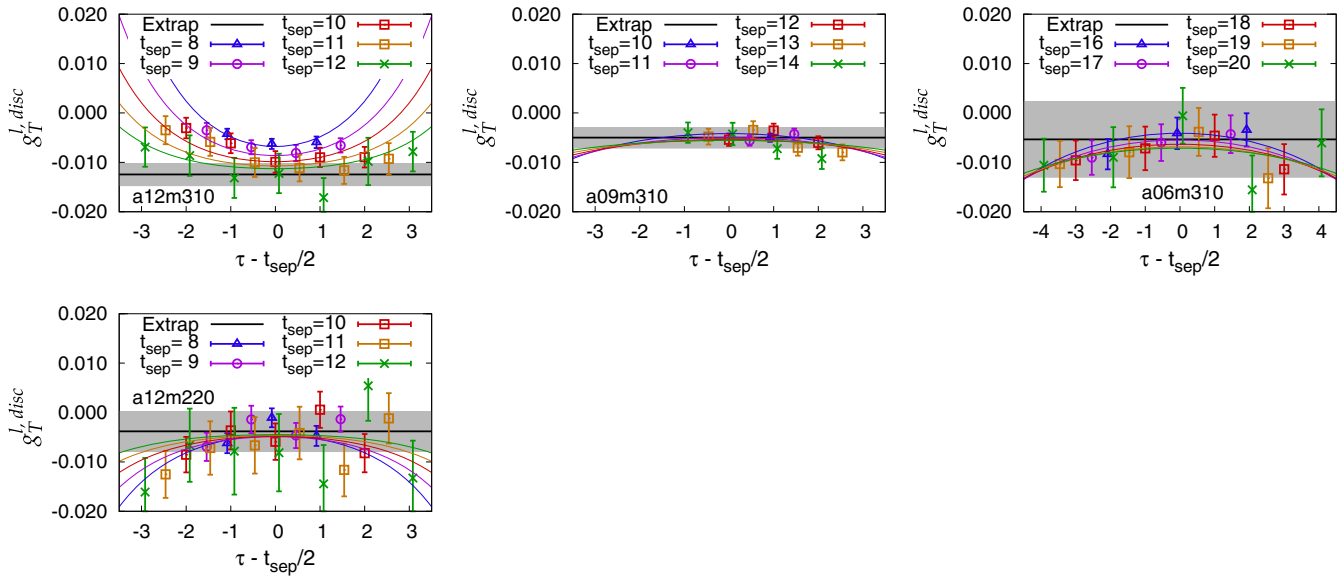

FIG. 7 (color online). Fits, using Eq. (11), to isolate the excited state contribution in the light quark disconnected diagram, $g_T^{\rm l,disc}$, are shown for the four ensembles analyzed. The solid black line and the grey band are the ground state estimate and error. The data and results of the fit for different $t_{\rm sep}$ are also shown.

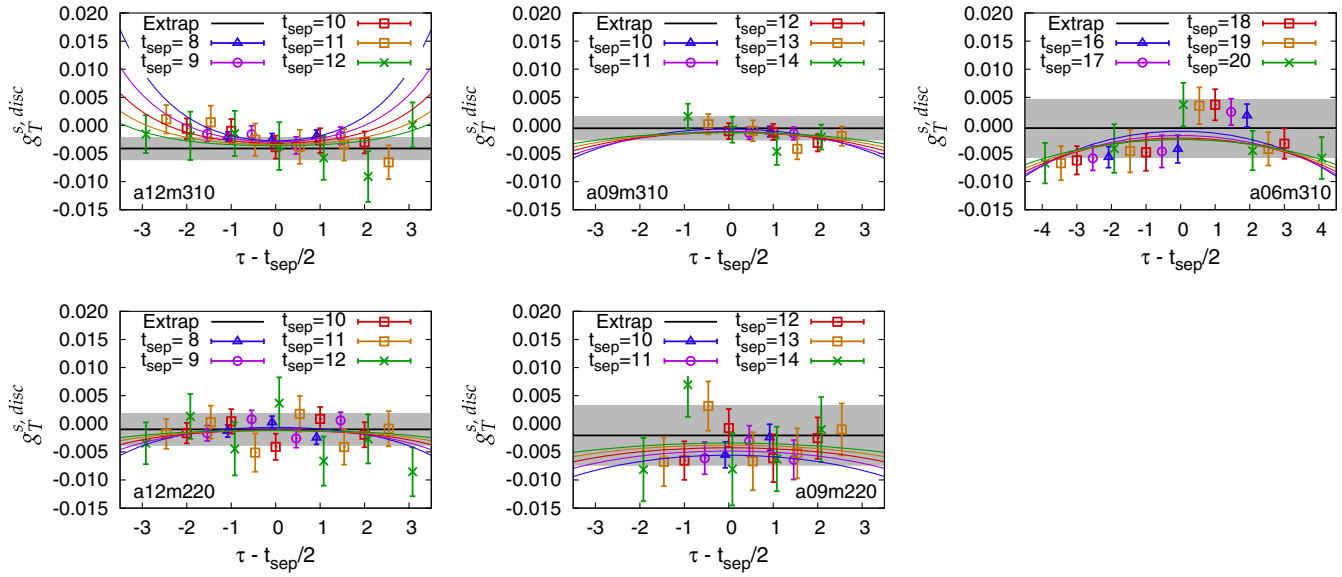

FIG. 8 (color online). Fits, using Eq. (11), to isolate the excited state contribution in the strange quark disconnected diagram, $g_T^{\rm s,disc}$, are shown for the five ensembles analyzed. The solid black line and the grey band are the ground state estimate and error. The data and results of the fit for different $t_{\rm sep}$ are also shown.

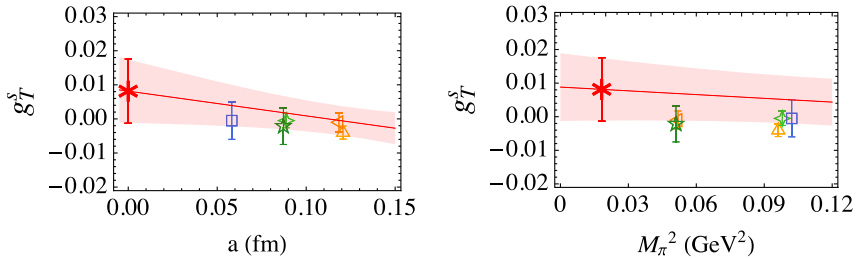

FIG. 9 (color online). Fits using Eq. (15) to obtain the result in the continuum limit ($a \to 0$) and at the physical pion mass ($M_\pi \to M_{\pi^0}^{\rm phys}$) of the strange quark disconnected contribution. A finite volume study was not carried out for the disconnected contribution. Rest is the same as in Fig. 4.

(100 [200]) of configurations analyzed as given in Table VIII.

Including the disconnected diagrams also requires calculating their contribution to the renormalization constants in the RI-sMOM scheme. We have not done this due to the poor signal in disconnected diagrams and use the same renormalization factor as calculated for the connected diagrams. In perturbation theory, the disconnected diagrams come in at higher order, so their contributions are expected to be small. Furthermore, the disconnected quark loop contributions themselves are very small for the nucleon tensor charges, so we expect the impact of the small difference in the renormalization factor due to neglecting the disconnected piece in Z_T will change the final estimate by much less than the statistical error quoted in Table VI. The final renormalized results, with this caveat, are given in Table VII.

There are two ways in which we can study the quark mass dependence of the disconnected contribution. First, by comparing the strange with light quark loop contributions we note that the estimates on all four ensembles increase as the quark mass is decreased. The second is to compare the estimates on the *a12m310* and *a12m220* ensembles. Unfortunately, the statistical errors in the latter are too large to draw a conclusion, even though we used the largest number of random sources per configuration for this study. Our conclusion is that a higher statistics study is needed to quantify the quark mass dependence and reduce the overall error in the disconnected contribution so that a reliable continuum extrapolation can be made.

The authors in Ref. [29] found that the disconnected contribution to the nucleon tensor charge is consistent with zero on a $N_f = 2 + 1 + 1$ twisted mass fermion ensemble at $a = 0.082(4)$ fm and $M_\pi = 370$ MeV. While a direct comparison with our results would be meaningful only after both results have been extrapolated to the continuum and physical pion mass limit, we note that our estimates are also consistent with zero for all ensembles with the strange quark loop, and in two of the four cases of light quark loops.

Given that the estimates of the disconnected contribution with light quark loops are small compared to connected part, have large errors, and have been obtained on only four ensembles, we do not include them in estimates of the isoscalar charges $g_T^{(u,d)}$. Instead, we take the largest value 0.0121 on the *a12m310* ensemble and use it as an estimate of the systematic error associated with neglecting the disconnected piece. This error is added in quadrature to the overall error in the connected estimate. The disconnected contribution with strange quark loops is even smaller but we keep it since it does not have a connected piece and we can perform a reasonable extrapolation in the lattice spacing and the quark mass as shown in Fig. 9, and get

$$g_T^{s,\rm disc} = 0.008(9), \tag{30}$$

with a $\chi^2/\text{dof} = 0.29$ for dof $= 2$. Bounding g_T^s is important for the analysis of the neutron EDM, especially if the chirality flip is controlled by the Higgs Yukawa coupling. In those beyond the standard model (BSM) scenarios, the contribution of g_T^s would be enhanced by the ratio of quark masses $m_s/m_{u,d}$ (i.e., proportional to the coupling of a "Higgs" to quarks), relative to g_T^u and g_T^d. Using these estimates, the analysis of the contribution of the quark EDMs to the neutron EDM is presented in Sec. V B.

V. NUCLEON TENSOR CHARGES AND QUARK ELECTRIC DIPOLE MOMENT

In the previous Secs. III and IV C, we discussed the calculation of the connected and disconnected diagrams to the nucleon tensor charges. In this section we present our final results for the nucleon tensor charges and the constraints they put on the quark EDM couplings using the current bound on the neutron EDM.

A. Nucleon tensor charge

The isovector tensor charge g_T^{u-d}, needed to probe novel tensor interactions at the TeV scale in the helicity-flip part of neutron decays, does not get any contributions from the disconnected diagram in the isospin symmetric limit that we are working under. We consider the extraction of g_T^{u-d} reliable because all systematics are under control. In particular, we find (i) that the fit ansatz in Eq. (11) converges, indicating that the excited state contamination has been isolated. (ii) the data for the renormalization constant in the RI-sMOM scheme shows a window in q^2 for

which the final estimates in the $\overline{\text{MS}}$ scheme at 2 GeV are constant within errors as discussed in Sec. II D. Finally (iii), the estimates on the nine ensembles show little dependence on the lattice spacing, pion mass and lattice volume as shown in Fig. 5 and discussed in Sec. III.

Our final estimate given in Eq. (17), $g_T^{u-d} = 1.020(76)$, is in good agreement with other lattice calculations by the LHPC ($N_f = 2+1$ HEX smeared clover action, domain wall action, and domain wall-on-asqtad actions) [30], RBC/UKQCD ($N_f = 2+1$ domain wall fermions [31], ETMC ($N_f = 2+1+1$ twisted mass fermions) [32–34] and the RQCD ($N_f = 2$ $O(a)$ improved clover fermions) [35] as shown in Fig. 12. A more detailed discussion of the systematics in these calculations and control over them using the FLAG quality criteria [6] is given in the Appendix.

An analysis of the extrapolation to the physical quark mass has also been carried out by the LHPC [30] and RQCD [35] collaborations. They did not find significant dependence on the lattice spacing and volume, so they extrapolate only in the quark mass using linear/quadratic (LHPC) and linear (RQCD) fits in M_π^2. Their final estimates, $g_T^{u-d} = 1.038(11)(12)$ (LHPC) and $g_T^{u-d} = 1.005(17)(29)$ (RQCD) are consistent with ours, but the size of our error is much larger. This is due to a combination of three factors in our calculation: (i) our determination of renormalization constants have larger uncertainty; (ii) errors in individual points are larger because they are the estimates in the $t_{\text{sep}} \to \infty$ limit obtained by extrapolating the data with multiple t_{sep} using a two state ansatz; and (iii) we extrapolate in all three variables using Eq. (15), whereas LHPC and RQCD extrapolate only in M_π^2. A fit to our data versus only M_π^2, also shown in Fig 6, gives a similarly accurate estimate $g_T^{u-d} = 1.059(29)$ with a $\chi^2/\text{dof} = 0.3$.

A comparison between recent lattice QCD results for g_T^{u-d} and estimates derived from model calculations and experimental data are summarized in Fig. 10.[2] The lattice estimates show consistency and little sensitivity to the number of flavors, i.e., $N_f = 2$ or $2+1$ or $2+1+1$, included in the generation of gauge configurations. The errors in model and phenomenological estimates (integral over the longitudinal momentum fraction of the experimentally measured quark transversity distributions) are large. Only the Dyson-Schwinger estimate (DSE'14) has comparable errors and lies about 4σ below the lattice QCD estimates.

To summarize, even with a very conservative error estimate, our result $g_T^{u-d} = 1.020(76)$, meets the target uncertainty of ∼10% required to bound novel tensor interactions using measurements of the helicity flip part of the neutron decay distribution in experiments planning to reach 10^{-3} accuracy. Our goal for the future is to reduce the error in g_S, which currently is ∼30% for the data sets presented in this work, to the same level.

[2]A similar comparison is presented in Ref. [36].

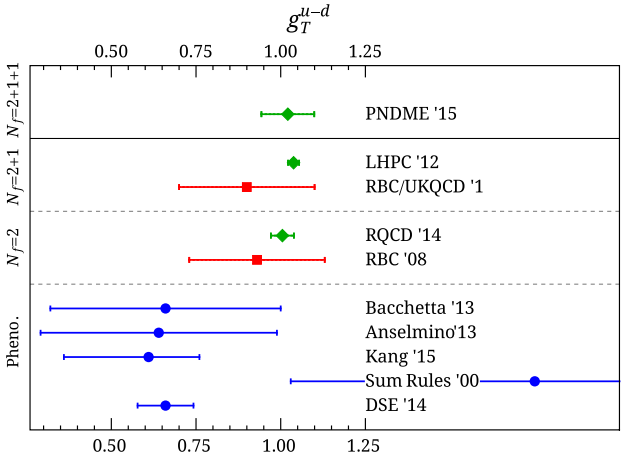

FIG. 10 (color online). A comparison between recent lattice QCD results for g_T^{u-d} and estimates derived from model calculations and experimental data. The published lattice QCD results are from LHPC'12 [30], RBC/UKQCD'10 [31], RQCD'14 [35] and RBC'08 [37]. Lattice estimates with reasonable control over excited state contamination and extrapolation to the physical pion mass and the continuum limit are shown in green. Estimates from models and phenomenology are from Bacchetta'13 [38], Anselmino'13 [39], Kang'15 [40], Sum Rules'00 [41], DSE'14 [42].

B. Quark electric dipole moment

The quark EDM contributions to the neutron EDM, d_n, are given by

$$d_n = d_u g_T^u + d_d g_T^d + d_s g_T^s \tag{31}$$

where the low-energy effective couplings d_u, d_d and d_s encapsulate the new CP violating interactions at the TeV scale. The goal of the analysis, knowing the charges g_T^q and a bound on d_n, is to constrain the couplings d_q and, in turn, BSM theories.

TABLE IX. A comparison of our lattice estimates of g_T^d and g_T^u of the proton with those from different models and phenomenology. The "Transversity 1" estimate is given both at the original scale at which it was evaluated (∼1 GeV) and after running to 2 GeV to show the magnitude of the scaling effect. The symbol "?" in the last column indicates that the scale at which the calculation is done is undetermined.

	g_T^d	g_T^u	g_T^s	μ
This study	−0.23(3)	0.77(7)	0.008(9)	2 GeV
Quark model	−1/3	4/3	⋯	⋯
QCD Sum Rules [41]	−0.35(17)	1.4(7)	⋯	?
Dyson-Schwinger [42]	−0.11(2)	0.55(8)	⋯	2 GeV
Transversity 1 [38]	−0.18(33)	0.57(21)	⋯	∼1 GeV
Transversity 1 [38]	−0.16(30)	0.51(19)	⋯	2 GeV
Transversity 2 [39]	−0.25(20)	0.39(15)	⋯	∼1 GeV
Transversity 3 [40]	$-0.22^{+0.14}_{-0.08}$	$0.39^{+0.07}_{-0.11}$	⋯	3.2 GeV

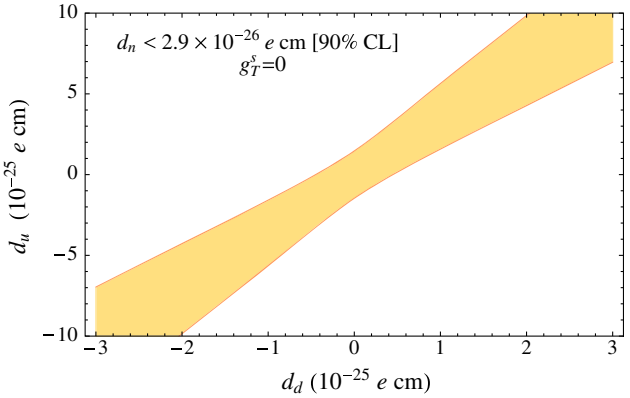

FIG. 11 (color online). Bounds on the couplings $d_{u,d}$ for the case $g_T^s = 0$. Estimates used for g_T^u and g_T^d are given in Eq. (32).

The calculation of the connected contribution to the g_T^q has been discussed in Sec. V A. Estimates of the disconnected contribution were discussed in Sec. IV C. Including the largest value (0.0121 obtained on the *a12m310* ensemble) as a systematic error, our final results in the $\overline{\text{MS}}$ scheme at 2 GeV for the nucleon charges that get contributions from the disconnected diagrams are

$$\begin{aligned} g_T^u &= 0.774(66), \\ g_T^d &= -0.233(28), \\ g_T^{u+d} &= 0.541(67). \end{aligned} \tag{32}$$

Note that incorporating the disconnected contribution as a systematic error increases the errors marginally as can be seen by comparing estimates in Eq. (32) with those in Eq. (16). Results for the neutron tensor charges are obtained by using the isospin symmetry, i.e., by interchanging the labels $u \leftrightarrow d$.

These final estimates are significantly smaller in magnitude than the quark model values, $g_T^u = 4/3$ and $g_T^d = -1/3$, but consistent with estimates derived from model calculations and experimental data summarized in Table IX.[3] The three phenomenological estimates Bacchetta'13 [38], Anselmino'13 [39], and Kang'15 [40] give consistent but lower estimates for g_T^u and g_T^d with $g_T^{u-d} \sim 0.65$. Similarly, taking the errors at face value, the Schwinger-Dyson estimate is $\sim 4\sigma$ below the lattice QCD results. A recent reevaluation of the calculation of tensor charges using QCD sum rules with input from lattice QCD has been reported in [44,45]. Their estimates in the $\overline{\text{MS}}$ scheme at 1 GeV are $g_T^d = 0.79$ and $g_T^u = -0.20$, each with $\approx 50\%$ uncertainty. Run to 2 GeV, these estimates would decrease by $\approx 10\%$ in magnitude. These results are consistent with ours given in (32) but place less stringent constraints on the neutron EDM and BSM theories due to the larger uncertainty.

Assuming that only the EDMs of the u, d, and s quarks contribute to the neutron EDM via Eq. (31) and the values of $g_T^{u,d,s}$ are given by Eqs. (32) and (30), one can put bounds on the $d_{u,d,s}$. Using the current estimate $|d_N| < 2.9 \times 10^{-26}\ e$ cm (90% C.L.) [46], 1-sigma slab priors for g_T^u and g_T^d given in Eq. (32), and assuming $g_T^s = 0$, we obtain the 90% confidence interval bounds for d_u and d_d shown in Fig. 11. Note that d_s is not constrained since g_T^s is consistent with zero.

Using these estimates of $g_T^{u,d,s}$, we have analyzed the consequences on split SUSY models, in which the quark EDM is the leading contribution in [5]. Our goal for the future is to improve the estimates presented here and develop the lattice methodology to include the contributions of the quark chromoelectric dipole moment operator.

VI. CONCLUSIONS

We have presented a high statistics study of the isovector and isoscalar tensor charges of the nucleon using clover-on-HISQ lattice QCD. We calculate both the connected and disconnected diagrams contributing to these charges. The analysis of nine ensembles covering the range 0.12–0.06 fm in lattice spacing, $M_\pi = 130$–320 MeV in pion mass, and $M_\pi L = 3.2$–5.4 in lattice volume allowed us to control the various sources of systematic errors. We show that keeping one excited state in the analysis allows us to isolate and mitigate excited state contamination. The renormalized estimates of the various tensor charges show small dependence on the lattice volume, lattice spacing and the light quark mass. These results can, therefore, be extrapolated reliably to the physical point.

Our final estimate for the tensor charge $g_T^{u-d} = 1.020(76)$ is in good agreement with previously reported estimates. The signal in the calculation of the disconnected diagrams is weak in spite of using state-of-the-art error reduction techniques. The value is small and we bound its contribution to light quark charges g_T^u and g_T^d. The signal for strange disconnected loop is even smaller, however in this case we are able to extrapolate the results to the continuum limit and find $g_T^s = 0.008(9)$. Using these estimates and the current bound on the neutron electric dipole moment, we carry out a first lattice QCD analysis of the constraints on the strengths of the up, down and strange quark electric dipole moments. The impact of these constraints on the viability of split SUSY models, in which the quark EDM is the leading contribution to the neutron EDM, is carried out in [5].

ACKNOWLEDGMENTS

We thank the MILC Collaboration for providing the $2+1+1$ flavor HISQ lattices used in our calculations. Simulations were carried out on computer facilities of (i) the USQCD Collaboration, which are funded by the Office of Science of the U.S. Department of Energy, (ii) the

[3]The effect of the choice of scale μ is illustrated by converting the results in Ref. [38] from $\mu = 1$ GeV to $\mu = 2$ GeV using two-loop running with the anomalous dimensions taken from Refs. [20,43].

Extreme Science and Engineering Discovery Environment (XSEDE), which is supported by National Science Foundation Grant No. ACI-1053575, (iii) the National Energy Research Scientific Computing Center, a DOE Office of Science User Facility supported by the Office of Science of the U.S. Department of Energy under Contract No. DE-AC02-05CH11231; and (iv) Institutional Computing at Los Alamos National Laboratory. The calculations used the Chroma software suite [12]. This material is based upon work supported by the U.S. Department of Energy, Office of Science of High Energy Physics under Contract No. DE-KA-1401020 and the LANL LDRD program. The work of H. W. L. and S. D. C. was supported by DOE Grant No. DE-FG02-97ER4014. We thank Gunnar Bali, Martha Constantinou and Jeremy Green for providing their latest data, and Emanuele Mereghatti for discussions on the chiral extrapolation. We thank Constantia Alexandrou, Gunnar Bali, Tom Blum, Shigemi Ohta, Dirk Pleiter and the LHP collaboration for discussions on the FLAG analysis.

APPENDIX: SYSTEMATICS IN THE CALCULATION OF THE ISOVECTOR NUCLEON TENSOR CHARGE

In Table X, we give a summary, in the FLAG format [47], of the level of control over various systematics in the calculation of the isovector tensor charge of the nucleon using simulations of lattice QCD with $N_f = 2$, $2+1$ and $2+1+1$ flavors. Note that a community wide consensus on applying the FLAG criteria to matrix elements within nucleon states does not yet exist. By performing this analysis, we wish to emphasize that the agreement between various calculations of g_T^{u-d} has reached a level of precision that calls for a FLAG like analysis.

The systematics covered by the FLAG criteria are also encountered in the calculation of matrix elements within

TABLE X. A summary of the control over various sources of systematic errors in lattice QCD calculations of the isovector tensor charge g_T^{u-d} using the FLAG quality criteria [6] reproduced in this Appendix. Results from all collaborations quoted in this table have used nonperturbative methods for calculating the renormalization constants.

Collaboration	Ref.	publication status	N_f	chiral extrapolation	continuum extrapolation	finite volume	excited state	renormalization	g_T
PNDME'15	This work	P	$2+1+1$	★	★	★	★	★	1.020(76)[a]
ETMC'15	[34]	P	$2+1+1$	■	■	★	★	★	1.053(21)[b]
LHPC'12	[30]	A	$2+1$	★	○	★	○	★	1.038(11)(12)[c]
RBC/UKQCD'10	[31]	A	$2+1$	○	■	★	■	★	0.9(2)[d]
RQCD'14	[35]	A	2	★	★	★	○	★	1.005(17)(29)[e]
ETMC'15	[34]	P	2	★	■	■	★	★	1.027(62)[f]
RBC'08	[37]	A	2	■	■	★	■	★	0.93(6)[g]

[a]This estimate is obtained from a simultaneous fit versus a, M_π^2, and $e^{-M_\pi L}$ defined in Eq. (15) using data on nine clover-on-HISQ ensembles given in Table VII.

[b]The quoted estimate [34] is from a single $M_\pi = 373$ MeV, $a = 0.082$ fm and $N_f = 2+1+1$ maximally twisted mass ensemble. Three values of $t_{\rm sep} \approx 1$, 1.15, and 1.3 fm are analyzed for handling excited state contamination. We quote their result from the two-state fit. A second low statistics study on an ensemble with $M_\pi = 213$ MeV and $a = 0.064$ fm gave a consistent estimate.

[c]The central value is from a two parameter chiral fit to just the coarse Wilson ensembles data. This agrees with a three parameter chiral fit to data from three different lattice actions simulated at different lattice spacings and with different volumes. Uncertainty due to extrapolation in the lattice spacing a and the finite volume controlled by $M_\pi L$ is expected to be small.

[d]Result is based on simulations at one lattice spacing $1/a = 1.73$ GeV using domain wall fermions. The statistics for the ensembles corresponding to the four pion masses simulated, $M_\pi = 329$, 416, 550, 668 MeV, were 3728, 1424, 392, 424 measurements, respectively. A single $t_{\rm sep} = 1.39$ fm was used.

[e]The result of this clover-on-clover study is obtained using a fit linear in M_π^2 keeping data with $M_\pi^2 < 0.1$ GeV^2 only. Data do not show significant dependence on lattice spacing or lattice volume. Excited state study is done on three of the eleven ensembles. Most of the data are with $t_{\rm sep} \sim 1$ fm. The second error is an estimate of the discretization errors assuming they are $O(a^2)$ since $O(a)$ improved operators with 1-loop estimates for the improvement coefficients are used in calculations done on $a = 0.081$, 0.071 and 0.06 fm lattices. Preliminary estimates presented by the QCDSF collaboration [48] are superseded by this publication [49].

[f]Result from a single ensemble of maximally twisted mass fermions with a clover term at $a = 0.093(1)$ fm, $M_\pi = 131$ MeV and $M_\pi L \approx 3$. To control excited state contamination, three values of $t_{\rm sep} \approx 0.94$, 1.1 and 1.3 fm are analyzed. We quote their value from the $t_{\rm sep} \approx 1.3$ fm analysis.

[g]Results based on one lattice spacing $1/a = 1.7$ GeV with the DBW2 domain wall action, three values of quark masses with $M_\pi = 493$, 607, 695 MeV, and $O(500)$ measurements. Only one $t_{\rm sep} = 10$ (1.14 fm) was simulated except at the lightest mass where $t_{\rm sep} = 12$ data was generated but used only as a consistency check as it has large errors.

baryon states. We, therefore, follow the same quality criteria for the publication status, chiral extrapolation, finite volume effects, and renormalization as defined by FLAG [6] and define an additional criterion, excited state contamination, that is relevant to the calculations of matrix elements within nucleon states. For the criterion "continuum extrapolation" we relax the requirement of an extrapolation provided the data meet the rest of the requirements: do not warrant an extrapolation, and a reasonable estimate of the uncertainty is provided. We also do not require that the action and the operators are $O(a)$ improved.

(i) Publication status:
- A published or plain update of published results
- P preprint
- C conference contribution

(ii) Chiral extrapolation:
- ★ $M_{\pi,\mathrm{min}} < 200$ MeV
- ○ 200 MeV $\leq M_{\pi,\mathrm{min}} \leq 400$ MeV
- ■ 400 MeV $< M_{\pi,\mathrm{min}}$

(iii) Continuum extrapolation:
- ★ 3 or more lattice spacings, at least 2 points below 0.1 fm
- ○ 2 or more lattice spacings, at least 1 point below 0.1 fm
- ■ otherwise

(iv) Finite-volume effects:
- ★ $M_{\pi,\mathrm{min}}L > 4$ or at least 3 volumes
- ○ $M_{\pi,\mathrm{min}}L > 3$ and at least 2 volumes
- ■ otherwise

(v) Renormalization:
- ★ nonperturbative
- ○ 1-loop perturbation theory or higher with a reasonable estimate of truncation errors
- ■ otherwise

(vi) Excited State:
- ★ $t_{\mathrm{sep,max}} > 1.5$ fm or at least 3 source-sink separations, t_{sep}, investigated at each lattice spacing and at each M_π.
- ○ At least 2 source-sink separations with 1.2 fm $\leq t_{\mathrm{sep,max}} \leq 1.5$ fm at least one M_π at each lattice spacing.
- ■ otherwise

Plots of the data summarized in Table X, as a function of a, M_π^2 and $M_\pi L$ are shown in Fig. 12. One observes very little sensitivity to these three variables and on the number of fermion flavors or the lattice action used.

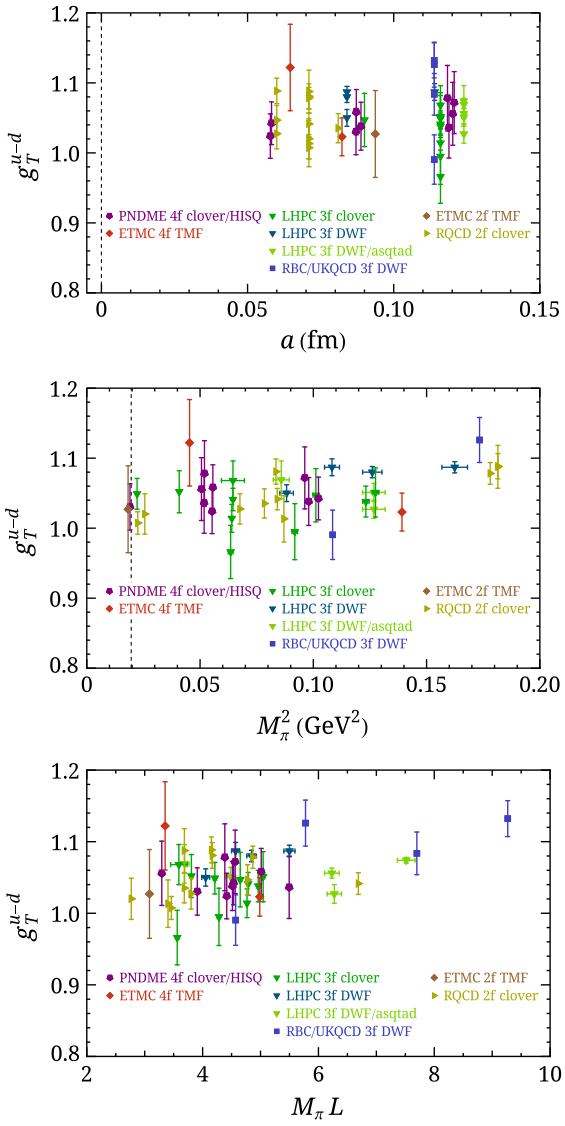

FIG. 12 (color online). Estimates of g_T^{u-d} from lattice QCD for $N_f = 2$, $2+1$ and $2+1+1$ flavors from the PNDME'15 (this work), ETMC'15 [32–34] LHPC'12 [30], RBC/UKQCD'10 [31], and RQCD'14 [35] collaborations. These data show little sensitivity to a (top), M_π^2 (middle), $M_\pi L$ (bottom) and on whether the strange and charm quarks are included in the generation of the lattice ensembles or on the lattice action used. The vertical dashed line in the middle panel marks the physical pion mass $M_\pi = 135$ MeV.

[1] T. Bhattacharya, V. Cirigliano, S. D. Cohen, A. Filipuzzi, M. González-Alonso, M. L. Graesser, R. Gupta, and Huey-Wen Lin, Phys. Rev. D **85**, 054512 (2012).

[2] H.-W. Lin, *Proc. Sci.*, LATTICE2012 (2012) 013 [arXiv:1212.6849].

[3] S. Syritsyn, *Proc. Sci.*, LATTICE2013 (2014) 009 [arXiv:1403.4686].

[4] M. Constantinou, *Proc. Sci.*, LATTICE2014 (2014) 001 [arXiv:1411.0078].

[5] T. Bhattacharya, V. Cirigliano, R. Gupta, H.-W. Lin, and B. Yoon, arXiv:1506.04196 [Phys. Rev. Lett. (to be published)].

[6] The Flavor Lattice Averaging Group (FLAG), http://itpwiki.unibe.ch/flag/images/1/16/FLAG_criteria.pdf (2015), FLAG quality criteria.

[7] E. Follana, Q. Mason, C. Davies, K. Hornbostel, G. P. Lepage, J. Shigemitsu, H. Trottier, and K. Wong (HPQCD Collaboration and UKQCD Collaboration), Phys. Rev. D **75**, 054502 (2007).

[8] A. Bazavov *et al.* (MILC Collaboration), Phys. Rev. D **87**, 054505 (2013).

[9] A. Hasenfratz and F. Knechtli, Phys. Rev. D **64**, 034504 (2001).

[10] T. Bhattacharya, S. D. Cohen, R. Gupta, A. Joseph, Huey-Wen Lin, and B. Yoon, Phys. Rev. D **89**, 094502 (2014).

[11] R. A. Briceno, H.-W. Lin, and D. R. Bolton, Phys. Rev. D **86**, 094504 (2012).

[12] R. G. Edwards and B. Joo (SciDAC Collaboration, LHPC Collaboration, and UKQCD Collaboration), Nucl. Phys. B, Proc. Suppl. **140**, 832 (2005).

[13] M. Clark, R. Babich, K. Barros, R. Brower, and C. Rebbi, Comput. Phys. Commun. **181**, 1517 (2010).

[14] T. Yamazaki, Y. Aoki, T. Blum, H.-W. Lin, S. Ohta, S. Sasaki, R. Tweedie, and J. Zanotti, Phys. Rev. D **79**, 114505 (2009).

[15] S. Collins, G. Bali, and A. Schafer, *Proc. Sci.*, LAT2007 (2007) 141 [arXiv:0709.3217].

[16] G. S. Bali, S. Collins, and A. Schafer, Comput. Phys. Commun. **181**, 1570 (2010).

[17] T. Blum, T. Izubuchi, and E. Shintani, Phys. Rev. D **88**, 094503 (2013).

[18] T. Bhattacharya, V. Cirigliano, R. Gupta, H.-W. Lin, and B. Yoon (to be published).

[19] G. Martinelli, C. Pittori, C. T. Sachrajda, M. Testa, and A. Vladikas, Nucl. Phys. **B445**, 81 (1995).

[20] C. Sturm, Y. Aoki, N. H. Christ, T. Izubuchi, C. T. C. Sachrajda, and A. Soni, Phys. Rev. D **80**, 014501 (2009).

[21] J. de Vries, R. Timmermans, E. Mereghetti, and U. van Kolck, Phys. Lett. B **695**, 268 (2011).

[22] R. Babich, J. Brannick, R. C. Brower, M. A. Clark, T. A. Manteuffel, S. F. McCormick, J. C. Osborn, and C. Rebbi, Phys. Rev. Lett. **105**, 201602 (2010).

[23] J. Osborn, R. Babich, J. Brannick, R. Brower, M. Clark *et al.*, *Proc. Sci.*, LATTICE2010 (2010) 037 [arXiv:1011.2775].

[24] C. Thron, S. Dong, K. Liu, and H. Ying, Phys. Rev. D **57**, 1642 (1998).

[25] C. Michael, M. Foster, and C. McNeile (UKQCD collaboration), Nucl. Phys. B, Proc. Suppl. **83**, 185 (2000).

[26] S. Bernardson, P. McCarthy, and C. Thron, Nucl. Phys. B, Proc. Suppl. **34**, 759 (1994).

[27] J. Viehoff, N. Eicker, S. Güsken, H. Hoeber, P. Lacock, Th. Lippert, K. Schilling, A. Spitz, and P. Ueberholz (TXL Collaboration), Nucl. Phys. B, Proc. Suppl. **63**, 269 (1998).

[28] J. Foley, K. J. Juge, A. Ó Cais, M. Peardon, S. M. Ryan, and Jon-Ivar Skullerud, Comput. Phys. Commun. **172**, 145 (2005).

[29] A. Abdel-Rehim, C. Alexandrou, M. Constantinou, V. Drach, K. Hadjiyiannakou, K. Jansen, G. Koutsou, and A. Vaquero, Phys. Rev. D **89**, 034501 (2014).

[30] J. R. Green, J. W. Negele, A. V. Pochinsky, S. N. Syritsyn, M. Engelhardt, and S. Krieg, Phys. Rev. D **86**, 114509 (2012).

[31] Y. Aoki, T. Blum, Huey-Wen Lin, S. Ohta, S. Sasaki, R. Tweedie, J. Zanotti, and T. Yamazaki, Phys. Rev. D **82**, 014501 (2010).

[32] C. Alexandrou, M. Constantinou, K. Jansen, G. Koutsou, and H. Panagopoulos, *Proc. Sci.*, LATTICE2013 (2014) 294 [arXiv:1311.4670].

[33] C. Alexandrou, M. Constantinou, K. Hadjiyiannakou, K. Jansen, C. Kallidonis *et al.*, *Proc. Sci.*, LATTICE2014 (2015) 151 [arXiv:1411.3494].

[34] A. Abdel-Rehim *et al.*, arXiv:1507.04936.

[35] G. S. Bali, S. Collins, B. Gläßle, M. Göckeler, J. Najjar, R. H. Rödl, A. Schäfer, R. W. Schiel, W. Söldner, and A. Sternbeck, Phys. Rev. D **91**, 054501 (2015).

[36] A. Courtoy, S. Baessler, M. Gonzalez-Alonso, and S. Liuti, arXiv:1503.06814 [Phys. Rev. Lett. (to be published)].

[37] H.-W. Lin, T. Blum, S. Ohta, S. Sasaki, and T. Yamazaki, Phys. Rev. D **78**, 014505 (2008).

[38] A. Bacchetta, A. Courtoy, and M. Radici, J. High Energy Phys. 03 (2013) 119.

[39] M. Anselmino, M. Boglione, U. D'Alesio, S. Melis, F. Murgia, and A. Prokudin, Phys. Rev. D **87**, 094019 (2013).

[40] Z.-B. Kang, A. Prokudin, P. Sun, and F. Yuan, arXiv:1505.05589.

[41] M. Pospelov and A. Ritz, Phys. Lett. B **471**, 388 (2000).

[42] M. Pitschmann, C.-Y. Seng, C. D. Roberts, and S. M. Schmidt, Phys. Rev. D **91**, 074004 (2015).

[43] J. Gracey, Phys. Lett. B **488**, 175 (2000).

[44] K. Fuyuto, J. Hisano, N. Nagata, and K. Tsumura, J. High Energy Phys. 12 (2013) 010.

[45] J. Hisano, J. Y. Lee, N. Nagata, and Y. Shimizu, Phys. Rev. D **85**, 114044 (2012).

[46] C. Baker, D. Doyle, P. Geltenbort, K. Green, M. van der Grinten *et al.*, Phys. Rev. Lett. **97**, 131801 (2006).

[47] The Flavor Lattice Averaging Group (FLAG), http://itpwiki.unibe.ch/flag/index.php/Review_of_lattice_results_concerning_low_energy_particle_physics (2015).

[48] D. Pleiter *et al.* (QCDSF/UKQCD), *Proc. Sci.*, LATTICE2010 (2010) 153 [arXiv:1101.2326].

[49] S. Collins and D. Pleiter (private communication).